
This is an electronic reprint of the original article.
This reprint may differ from the original in pagination and typographic detail.

Hovatta, T.; MAGIC Collaboration; MWL Collaborators

The variability patterns of the TeV blazar PG 1553 + 113 from a decade of MAGIC and multiband observations

Published in:
Monthly Notices of the Royal Astronomical Society

DOI:
[10.1093/mnras/stae649](https://doi.org/10.1093/mnras/stae649)

Published: 01/04/2024

Document Version
Publisher's PDF, also known as Version of record

Published under the following license:
CC BY

Please cite the original version:
Hovatta, T., MAGIC Collaboration, & MWL Collaborators (2024). The variability patterns of the TeV blazar PG 1553 + 113 from a decade of MAGIC and multiband observations. *Monthly Notices of the Royal Astronomical Society*, 529(4), 3894-3911. <https://doi.org/10.1093/mnras/stae649>

This material is protected by copyright and other intellectual property rights, and duplication or sale of all or part of any of the repository collections is not permitted, except that material may be duplicated by you for your research use or educational purposes in electronic or print form. You must obtain permission for any other use. Electronic or print copies may not be offered, whether for sale or otherwise to anyone who is not an authorised user.

The variability patterns of the TeV blazar PG 1553 + 113 from a decade of MAGIC and multiband observations

MAGIC Collaboration: H. Abe,^{1★} S. Abe,¹ J. Abhir,² V. A. Acciari,³ I. Agudo,⁴ T. Aniello,⁵ S. Ansoldi,^{6,7} L. A. Antonelli,⁵ A. Arbet Engels,⁸ C. Arcaro,⁹ M. Artero,¹⁰ K. Asano,¹ D. Baack,¹¹ A. Babić,¹² A. Baquero,¹³ U. Barres de Almeida,¹⁴ I. Batković,⁸ J. Baxter,¹ J. Becerra González,³ E. Bernardini,⁸ J. Bernete,¹⁵ A. Berti,⁷ J. Besenrieder,⁷ C. Bigongiari,⁵ A. Biland,² O. Blanch,⁹ G. Bonnoli,⁵ Ž. Bošnjak,¹² I. Burelli,⁶ G. Busetto,⁸ A. Campoy-Ordaz,¹⁶ A. Carosi,⁵ R. Carosi,¹⁷ M. Carretero-Castrillo,¹⁸ A. J. Castro-Tirado,⁴ Y. Chai,⁷ A. Cifuentes,¹⁵ S. Cikota,¹² E. Colombo,³ J. L. Contreras,¹³ J. Cortina,¹⁵ S. Covino,⁵ G. D’Amico,¹⁹ V. D’Elia,⁵ P. Da Vela,^{17,20} F. Dazzi,⁵ A. De Angelis,⁸ B. De Lotto,⁶ A. Del Popolo,²¹ M. Delfino,^{9,22} J. Delgado,^{9,22} C. Delgado Mendez,¹⁵ D. Depaoli,²³ F. Di Piero,²³ L. Di Venere,²⁴ D. Dominis Prester,²⁵ A. Donini,⁵ D. Dorner,² M. Doro,⁹ D. Elsaesser,^{11,26} G. Emery,²⁷ J. Escudero,⁴ L. Fariña,⁹ A. Fattorini,¹¹ L. Foffano,⁵ L. Font,¹⁶ S. Fukami,² Y. Fukazawa,²⁸ R. J. García López,³ S. Gasparyan,²⁹ M. Gaug,¹⁶ J. G. Giesbrecht Paiva,¹⁴ N. Giglietto,²⁴ F. Giordano,²⁴ P. Gliwny,³⁰ R. Grau,⁹ J. G. Green,⁸ D. Hadasch,¹ A. Hahn,⁸ L. Heckmann,^{8,31} J. Herrera,³ T. Hovatta,^{32,33★} D. Hrupec,³⁴ M. Hütten,¹ R. Imazawa,²⁸ T. Inada,¹ R. Iotov,³⁵ K. Ishio,³⁰ I. Jimenez Martínez,¹⁵ J. Jormanainen,³² D. Kerszberg,⁹ G. W. Kluge,^{19,36} Y. Kobayashi,¹ P. M. Kouch,³² H. Kubo,¹ J. Kushida,³⁷ M. Láinez Lezáun,¹² A. Lamastra,⁵ F. Leone,⁵ E. Lindfors,³² I. Liodakis,^{32,38} S. Lombardi,⁵ F. Longo,^{6,39} M. López-Moya,¹³ A. López-Oramas,³ S. Loporchio,²⁴ A. Lorini,⁴⁰ B. Machado de Oliveira Fraga,¹⁴ P. Majumdar,⁴¹ M. Makariev,⁴² G. Maneva,⁴² N. Mang,¹¹ M. Manganaro,²⁵ K. Mannheim,^{26,35} M. Mariotti,⁹ M. Martínez,¹⁰ M. Martínez-Chicharro,¹⁵ A. Mas-Aguilar,¹³ D. Mazin,^{1,43} S. Menchiari,⁴⁰ S. Mender,¹¹ D. Miceli,⁹ T. Miener,¹³ J. M. Miranda,⁴⁰ R. Mirzoyan,⁸ M. Molero González,³ E. Molina,³ H. A. Mondal,⁴¹ A. Moralejo,¹⁰ D. Morcuende,¹³ T. Nakamori,⁴⁴ C. Nanci,⁵ V. Neustroev,⁴⁵ C. Nigro,¹⁰ L. Nikolić,⁴⁰ K. Nilsson,³² K. Nishijima,³⁷ T. Njoh Ekoume,³ K. Noda,⁴⁶ S. Nozaki,⁷ Y. Ohtani,¹ A. Okumura,⁴⁷ J. Otero-Santos,³ S. Paiano,⁵ M. Palatiello,⁶ D. Paneque,⁸ R. Paoletti,⁴⁰ J. M. Paredes,¹⁸ D. Pavlović,²⁵ M. Persic,^{6,48} M. Pihet,⁹ G. Pirola,⁸ F. Podobnik,⁴⁰ P. G. Prada Moroni,¹⁷ E. Prandini,⁹ G. Principe,⁶ C. Priyadarshi,¹⁰ W. Rhode,¹¹ M. Ribó,¹⁸ J. Rico,¹⁰ C. Righi,⁵ N. Sahakyan,²⁹ T. Saito,¹ K. Satalecka,³² F. G. Saturni,⁵ B. Schleicher,³⁵ K. Schmidt,¹¹ F. Schmuckermaier,⁸ J. L. Schubert,¹¹ T. Schweizer,⁸ A. Sciacaluga,⁵ J. Sitarek,³⁰ A. Spolon,⁹ A. Stamerra,^{5★} J. Strišćković,³⁴ D. Strom,⁸ Y. Suda,²⁸ S. Suutarinen,³² H. Tajima,⁴⁷ R. Takeishi,¹ F. Tavecchio,⁵ P. Temnikov,⁴² K. Terauchi,⁴⁹ T. Terzić,²⁵ M. Teshima,^{8,50} L. Tosti,⁵¹ S. Truzzi,⁴⁰ A. Tutone,⁵ S. Ubach,¹⁶ J. van Scherpenberg,⁸ S. Ventura,⁴⁰ V. Verguilo,⁴² I. Viale,⁹ C. F. Vigorito,²³ V. Vitale,⁵² R. Walter,²⁷ C. Wunderlich,⁴⁰ T. Yamamoto,⁵³ MAGIC collaborators: H. Jermak,⁵⁴ I. A. Steele,⁵⁴ P. S. Smith,⁵⁵ D. Blinov,^{56,57} C. M. Raiteri,⁵⁸ M. Villata,⁵⁸ D. O. Mirzaqulov,⁵⁹ S. O. Kurtanidze,^{60,61} D. Carosati,^{62,63} S. S. Savchenko,^{64,65} J. A. Acosta-Pulido,³ G. A. Borman,⁶⁶ V. Bozhilov,⁶⁷ M. I. Carnerero,⁵⁸ R. A. Chigladze,⁶⁰ G. Damjanovic,⁶⁸ S. A. Ehgamberdiev,^{59,69} M. Feige,²⁶ T. S. Grishina,⁶⁴ A. C. Gupta,⁷⁰ V. A. Hagen-Thorn,⁶⁴ S. Ibryamov,⁷¹ R. Z. Ivanidze,⁶⁰ S. G. Jorstad,^{64,72} J. Kania,²⁶ G. N. Kimeridze,⁶⁰ E. N. Kopatskaya,⁶⁴ M. Kopp,²⁶ L. Kunkel,²⁶ O. M. Kurtanidze,^{60,61,73} V. M. Larionov,⁶⁴ E. G. Larionova,⁶⁴ L. V. Larionova,⁶⁴ C. Lorey,²⁶ A. Marchini,⁷⁴ A. P. Marscher,⁷² M. Minev,⁷⁵ D. A. Morozova,⁶⁴ M. G. Nikolashvili,^{60,61} E. Ovcharov,⁶⁷ D. Reinhart,²⁶ A. C. Sadun,⁷⁶ A. Scherbantín,²⁶ L. Schneider,²⁶ E. Semkov,⁷⁵ L. A. Sigua,⁶⁰ R. Steineke,²⁶ Yu. V. Troitskaya,⁶⁴

* E-mail: contact.magic@mpp.mpg.de

I. S. Troitskiy,⁶⁴ A. Valcheva,⁶⁷ A. A. Vasilyev,⁶⁴ O. Vince,⁶⁸ E. Zaharieva,⁶⁷ N. Zottmann,²⁶ S. Kiehlmann,^{56,57} A. Readhead,^{56,77} W. Max-Moerbeck,⁷⁸ R. A. Reeves,⁷⁹ A. Sandrinelli,⁸⁰ V. Fallah Ramazani,^{32,33} M. Giroletti,⁸¹ S. Righini,⁸¹ N. Marchili,⁸¹ B. Patricelli,^{5,17} G. Ghirlanda^{80,82} and R. Lico⁸¹

Affiliations are listed at the end of the paper

Accepted 2024 February 27. Received 2024 February 13; in original form 2023 August 8

ABSTRACT

PG 1553 + 113 is one of the few blazars with a convincing quasi-periodic emission in the gamma-ray band. The source is also a very high energy (VHE; > 100 GeV) gamma-ray emitter. To better understand its properties and identify the underlying physical processes driving its variability, the MAGIC Collaboration initiated a multiyear, multiwavelength monitoring campaign in 2015 involving the OVRO 40-m and Medicina radio telescopes, REM, KVA, and the MAGIC telescopes, *Swift* and *Fermi* satellites, and the WEBT network. The analysis presented in this paper uses data until 2017 and focuses on the characterization of the variability. The gamma-ray data show a (hint of a) periodic signal compatible with literature, but the X-ray and VHE gamma-ray data do not show statistical evidence for a periodic signal. In other bands, the data are compatible with the gamma-ray period, but with a relatively high p -value. The complex connection between the low- and high-energy emission and the non-monochromatic modulation and changes in flux suggests that a simple one-zone model is unable to explain all the variability. Instead, a model including a periodic component along with multiple emission zones is required.

Key words: radiation mechanisms: non-thermal – galaxies: active – BL Lacertae objects: individual: (PG 1553 + 113) – gamma-rays: galaxies.

1 INTRODUCTION

Variability on a wide range of time-scales is a common trait of active galactic nuclei (AGNs, see Hovatta & Lindfors 2019, for a recent review). Among AGNs, the blazar subclass is dominated by the emission from the relativistic outflow emerging from the supermassive black hole (SMBH) and structured in beamed jets, namely, forming a small angle with the observer. The relativistic beaming amplifies the observed radiation and results in a broad spectral energy distribution (SED) dominated by the non-thermal continuum, showing two main humps. The first peaks in the infrared (IR) to X-ray region, presumably originated by synchrotron radiation, and the second hump spans from the UV up to the TeV. Blazars are distinguishable by their flux variability, with a large amplitude – up to two orders of magnitude – and fast variations, down to a few minutes. Depending on the equivalent width (EW) of the absorption line in the optical band, blazars are further divided into Flat Spectrum Radio Quasars (FSRQs, $EW > 5 \text{ \AA}$) and BL Lac objects (BL Lacs, $EW < 5 \text{ \AA}$). The location of the synchrotron peak in blazars determines a further division into low- ($\nu_{\text{peak}}^S < 10^{14} \text{ Hz}$), intermediate- ($10^{14} < \nu_{\text{peak}}^S < 10^{15} \text{ Hz}$), and high-synchrotron peak ($\nu_{\text{peak}}^S > 10^{15} \text{ Hz}$) BL Lacs. The mechanisms driving the variability in blazars are still debated, and several different interpretations were suggested, related to the physical processes in the jet or in the accretion mechanism (e.g. Marscher 2016; Raiteri et al. 2017b, and references therein).

Jet emission models can be tested by looking at the variability pattern and correlations between the low-energy and high-energy humps of the SED (Falomo, Pian & Treves 2014; Lioudakis et al. 2019), built through contemporaneous multiwavelength (MWL) monitoring campaigns (Ulrich, Maraschi & Urry 1997).

In this framework, the discovery of regular and periodic patterns in otherwise apparently stochastic variability can provide a deeper insight into the underlying processes.

PG 1553 + 113 is one of the brightest HBL emitting at gamma-ray energies. The search of intervening absorption in its far-UV spectrum suggest a redshift in the range $0.413 < z < 0.56$ (Danforth et al. 2010, 2016). Recent optical/UV observations seems to converge on a value of 0.433 for the redshift of this source (Johnson et al. 2019; Dorigo Jones et al. 2022).

Its comparably large redshift entails a strong attenuation of the gamma-ray flux above energies $E > 250 \text{ GeV}$ due to pair production with photons of the extragalactic background light (EBL). Albeit this attenuation, PG 1553 + 113 is a well-known TeV gamma-ray emitter observed by all major imaging air Cherenkov telescopes (IACTs; Aleksić et al. 2012; Abramowski et al. 2015; Aliu et al. 2015).

The continuous gamma-ray light curve was measured with the Large Area Telescope (LAT) on board the *Fermi* Gamma-ray Space Telescope since 2008 and shows a clear signature of a periodic modulation of $2.18 \pm 0.08 \text{ yr}$ at $E > 100 \text{ MeV}$ and $E > 1 \text{ GeV}$, covering 3.5 cycles (Ackermann et al. 2015). The periodicity has < 1 per cent chance of being due to random variability. This was the first time such a periodicity has been found convincingly in a gamma-ray blazar. The signature has been confirmed by several other works even in recent times (e.g. Covino et al. 2020; Peñil et al. 2020). Optical fluxes correlate with gamma-ray emission at 99 per cent confidence and the optical light curve shows evidence for modulation of $2.06 \pm 0.05 \text{ yr}$ over 4.5 cycles.

The mechanisms underlying the daily/weekly variability typical of blazars and the claimed periodicity are not fully understood. The long-term monitoring of the variable light curves of such objects is a powerful tool for discovering such processes, and observations with a complete MWL coverage are needed to understand them.

The last years have witnessed the growth of new key observations of possible periodic behaviours in AGNs and blazars, evaluated with different methods Bhatta (e.g. 2017), Ait Benkhali et al. (e.g. 2020), and also Covino, Sandrinelli & Treves (2019) for a cautious approach. The source PG 1553 + 113 has been used extensively to this end (e.g. Sobacchi, Sormani & Stamerra 2017). The periodicity should be compared to the lifetime and duty cycle of AGN activity, generally assumed as 10^7 – 10^8 yr, or to episodic nuclear activity and jet formation $\sim 10^5$ yr (Haehnelt & Rees 1993; Konar et al. 2013). For this reason, any claim of periodicity must establish compelling statistical evidence emerging from stochastic fluctuations that can mimic a periodic pattern.

Because the emission of HBLs across the electromagnetic spectrum is dominated by the jet, the quasi-periodic modulation is most probably associated with the jet itself or with the processes at its base. In the latter case, disc perturbations or instabilities can induce a variation of the accretion rate advected to the jet, with quasi-periodic behaviour (e.g. Tchekhovskoy, Narayan & McKinney 2011). Among the possible interpretations, the modulation can be driven by the interaction of two SMBHs (see e.g. Ackermann et al. 2015, and references therein). Therefore, PG 1553 + 113 is a candidate for harbouring a close binary SMBH system with milli-pc separation in the early inspiral gravitational-wave driven regime prior to coalescence (see e.g. Tavani et al. 2018). However, different viable solutions are possible. The observed modulation can be related to the jet itself, such as jet precession or intrinsically rotating flow or helical jet, or to the process feeding the jet. Each interpretation may lead to different expectations about the evolution of the modulation at different wavelengths. Geometrical models, e.g. due to jet precession (Romero et al. 2000), rotation (Camenzind & Krockenberger 1992; Rieger & Mannheim 2000), or helical structure (Conway & Murphy 1993), would produce a quasi-periodic variation of the beaming factor due to the change of the viewing angle (Rieger 2004). Therefore, almost achromatic variability is expected at all wavelengths, or with clear correlations between different wavelengths (Villata & Raiteri 1999). To test this hypothesis, PG 1553 + 113 was monitored with the very long baseline array (VLBA) at 15, 24, and 43 GHz in the period 2015–2017, a full cycle of gamma-ray activity (Lico et al. 2020). VLBA data provided evidence of jet angle variations, indicating that geometric effects could play a role in the observed emission variability through Doppler boosting modulation. However, no clear connection was found between the observed variations and the quasi-periodic variability patterns reported in optical and gamma rays. Therefore, additional mechanisms are necessary to explain the variable broad-band emission.

Pulsating instabilities occurring in the disc can explain the quasi-periodicity, also in the case of a single SMBH (Honma, Matsumoto & Kato 1992), as in magnetically dominated and magnetically arrested accretion flows in the inner disc part (Tchekhovskoy, Narayan & McKinney 2011).

In case the observed periodicity is interpreted as a periodic perturbation due to the interaction with a secondary black hole, a double or multiple peak substructure is expected at different bands, resulting from the interaction of the secondary black hole with the accretion disc near the periastron (Lehto & Valtonen 1996). Such a structure is apparent in the optical light curve, and the detection of similar double peaks in the X-ray and gamma-ray light curves would confirm this interpretation.

PG 1553 + 113 is also known to be variable on a weekly time-scale (Abramowski et al. 2015; Aleksić et al. 2015; Aliu et al. 2015). The study of flaring episodes provided an important input

for the modelling of intrinsic emission from the source and was used as a probe of fundamental physics (Guo et al. 2021) and of the EBL (Acciari et al. 2019; Korochkin, Neronov & Semikoz 2020). Finally, the reported periodicity could be accidental due to stochastic background fluctuations, typically found in light curves of AGNs and blazars. For this reason, proper statistical approaches such as those discussed in Vaughan et al. (2003) are needed when studying long-term light curves (e.g. Covino, Sandrinelli & Treves 2019). Multiwavelength observations are needed to support the physical interpretation of the emission from the innermost regions of the blazar and its jet.

With the purpose of characterizing PG 1553 + 113 broad-band variability and testing physical scenarios, the MAGIC collaboration initiated a multiyear, MWL monitoring campaign in 2015. In the campaign, various instruments observing in the radio, infrared, optical (both photometry and polarimetry), UV, soft X-ray, and gamma-ray bands were involved. In this article we report the results of this campaign, including data from previous observations. The paper is structured as follows: in Section 2, we present the details of the MAGIC and MWL data analyses. Section 3 is dedicated to the characterization of the source variability, while Section 4 is focused on periodicity study of the data presented in the paper. In Section 5, the conclusions of this work are outlined.

2 MULTIWAVELENGTH DATA AND ANALYSIS

The MWL data used in this study span several orders of magnitude, from radio to VHE gamma rays. In this section, we give a brief description of the collected data and their analyses (from higher to lower frequencies), while in the following sections we report on the scientific interpretation of the data.

2.1 VHE gamma-ray data

MAGIC is a system of two IACTs located in La Palma, Canary Islands, at 2200 m asl. It observes VHE gamma rays from 50 GeV up to tens of TeV. The angular resolution at around 200 GeV energies at low zenith angles (0° – 30°), is $< 0.07^\circ$, while the energy resolution is 16 per cent (Aleksić et al. 2016b). From 2004 to 2009, MAGIC was composed of a single IACT, MAGIC-I (Baixeras et al. 2004).

The MAGIC data are a collection of images registered by the camera of each telescope and are processed with a standard analysis chain (Zanin et al. 2013).

Since its detection in 2004, MAGIC observed PG 1553 + 113 every year. In the first two years of observation (2005 and 2006) the data were affected by large systematic and statistical errors, therefore, in this work we consider only data taken from 2007 on, where an upgrade of the telescope readout sensibly increased its performances (Aleksić et al. 2016a). For the study, we use the dark night data from 2007 to 2017, including already published data from 2007, 2008, 2009, and 2012 campaigns Aleksić et al. (2012, 2015).

Table 1 summarizes the results of the MAGIC data analysis of the samples collected from 2007 to 2017. Data from 2010 on were analysed with monthly binning, while for previous data, the overall yearly sample is considered as reported in Aleksić et al. (2012). The total observation time is ~ 100 hours, non uniformly distributed across the years (third column). Average fluxes above 150 GeV in physical units and in Crab Nebula units.¹ are reported in columns

¹The Crab Unit (C.U.) used in this work is an arbitrary unit obtained by dividing the integral energy flux measured above a certain threshold by the

Table 1. Summary of MAGIC telescopes observations.

| Year | Month | Time [h] | Average Flux >150 GeV [cm ⁻² s ⁻¹] | $F_{>150 \text{ GeV}}$ C.U. ^a | f_0 [cm ⁻² s ⁻¹ TeV ⁻¹] | Γ |
|-------------------|----------|-------------|--|---|--|-------------------|
| 2007 ^b | | 11.5 | $(1.40 \pm 0.38) \times 10^{-11}$ | 4 % | $(1.1 \pm 0.3) \times 10^{-10}$ | 4.1 ± 0.3 |
| 2008 ^b | | 8.7 | $(3.70 \pm 0.47) \times 10^{-11}$ | 11 % | $(2.6 \pm 0.3) \times 10^{-10}$ | 4.3 ± 0.4 |
| 2009 ^b | | 8.5 | $(1.63 \pm 0.45) \times 10^{-11}$ | 5 % | $(1.3 \pm 0.2) \times 10^{-10}$ | 3.6 ± 0.5 |
| 2010 | March | 3.19 | $(1.71 \pm 0.31) \times 10^{-11}$ | 5 % | $(1.1 \pm 0.1) \times 10^{-10}$ | 3.8 ± 0.7 |
| | June | 2.85 | $(2.11 \pm 0.34) \times 10^{-11}$ | 6 % | $(1.8 \pm 0.2) \times 10^{-10}$ | 3.2 ± 0.7 |
| 2011 | March | 2.19 | $(4.77 \pm 0.61) \times 10^{-11}$ | 14 % | $(3.2 \pm 0.4) \times 10^{-10}$ | 3.4 ± 0.3 |
| 2012 | February | 1.94 | $(2.54 \pm 0.42) \times 10^{-11}$ | 8 % | $(1.8 \pm 0.3) \times 10^{-10}$ | 3.6 ± 0.4 |
| | March | 11.58 | $(3.77 \pm 0.27) \times 10^{-11}$ | 11 % | $(2.4 \pm 0.2) \times 10^{-10}$ | 3.6 ± 0.2 |
| | April | 8.87 | $(5.85 \pm 0.34) \times 10^{-11}$ | 18 % | $(3.3 \pm 0.2) \times 10^{-10}$ | 3.7 ± 0.1 |
| 2013 | April | 4.00 | $(5.13 \pm 0.37) \times 10^{-11}$ | 16 % | $(3.0 \pm 0.3) \times 10^{-10}$ | 3.5 ± 0.2 |
| | May | 2.52 | $(2.21 \pm 0.39) \times 10^{-11}$ | 7 % | $(1.7 \pm 0.2) \times 10^{-10}$ | 3.7 ± 0.3 |
| | June | 6.35 | $(4.22 \pm 0.28) \times 10^{-11}$ | 13 % | $(2.6 \pm 0.2) \times 10^{-10}$ | 3.1 ± 0.1 |
| 2014 | March | 1.97 | $(4.09 \pm 0.55) \times 10^{-11}$ | 12 % | $(3.0 \pm 0.4) \times 10^{-10}$ | 3.4 ± 0.4 |
| 2015 | January | 1.13 | $(5.98 \pm 0.80) \times 10^{-11}$ | 18 % | $(3.9 \pm 0.7) \times 10^{-10}$ | 4.5 ± 0.4 |
| | March | 4.72 | $(5.09 \pm 0.36) \times 10^{-11}$ | 15 % | $(3.2 \pm 0.2) \times 10^{-10}$ | 3.9 ± 0.1 |
| | April | 4.16 | $(5.59 \pm 0.40) \times 10^{-11}$ | 17 % | $(3.5 \pm 0.2) \times 10^{-10}$ | 3.9 ± 0.1 |
| | May | 3.65 | $(3.83 \pm 0.43) \times 10^{-11}$ | 12 % | $(2.3 \pm 0.2) \times 10^{-10}$ | 3.8 ± 0.3 |
| | June | 3.73 | $(2.51 \pm 0.35) \times 10^{-11}$ | 8 % | $(1.8 \pm 0.3) \times 10^{-10}$ | 3.5 ± 0.4 |
| | July | 3.64 | $(4.00 \pm 0.44) \times 10^{-11}$ | 12 % | $(2.3 \pm 0.3) \times 10^{-10}$ | 3.7 ± 0.2 |
| | August | 4.47 | $(1.70 \pm 0.39) \times 10^{-11}$ | 5 % | $(1.4 \pm 0.4) \times 10^{-10}$ | 3.9 ± 0.4 |
| 2016 | January | 0.96 | $(2.76 \pm 0.86) \times 10^{-11}$ | 8 % | n.a. ^c | n.a. ^c |
| | February | 2.35 | $(2.19 \pm 0.48) \times 10^{-11}$ | 7 % | $(1.4 \pm 0.3) \times 10^{-10}$ | 3.8 ± 0.9 |
| | March | 5.19 | $(2.31 \pm 0.30) \times 10^{-11}$ | 7 % | $(1.5 \pm 0.2) \times 10^{-10}$ | 3.4 ± 0.2 |
| | April-a | 4.16 | $(3.33 \pm 0.29) \times 10^{-11}$ | 10 % | $(1.9 \pm 0.2) \times 10^{-10}$ | 4.1 ± 0.2 |
| | April-b | 2.28 | n.a. | n.a. | n.a. | n.a. |
| | May | 10.37 | $(4.22 \pm 0.23) \times 10^{-11}$ | 13 % | $(2.6 \pm 0.1) \times 10^{-10}$ | 3.6 ± 0.1 |
| | June | 4.43 | $(5.81 \pm 0.38) \times 10^{-11}$ | 18 % | $(3.2 \pm 0.2) \times 10^{-10}$ | 3.7 ± 0.1 |
| | July | 5.68 | $(2.57 \pm 0.29) \times 10^{-11}$ | 8 % | $(1.7 \pm 0.2) \times 10^{-10}$ | 3.5 ± 0.2 |
| | August | 3.25 | $(2.25 \pm 0.38) \times 10^{-11}$ | 7 % | $(1.4 \pm 0.3) \times 10^{-10}$ | 3.2 ± 0.2 |
| 2017 | January | 3.15 | $(4.17 \pm 0.41) \times 10^{-11}$ | 13 % | $(2.4 \pm 0.2) \times 10^{-10}$ | 3.9 ± 0.2 |
| | February | 7.74 | $(2.39 \pm 0.22) \times 10^{-11}$ | 7 % | $(1.6 \pm 0.1) \times 10^{-10}$ | 4.1 ± 0.1 |
| | March | 6.44 | $(2.46 \pm 0.26) \times 10^{-11}$ | 7 % | $(1.5 \pm 0.1) \times 10^{-10}$ | 4.0 ± 0.1 |
| | April | 5.43 | $(2.77 \pm 0.27) \times 10^{-11}$ | 8 % | $(1.7 \pm 0.1) \times 10^{-10}$ | 3.8 ± 0.1 |
| | May | 5.67 | $(2.82 \pm 0.28) \times 10^{-11}$ | 8 % | $(1.8 \pm 0.1) \times 10^{-10}$ | 3.8 ± 0.1 |
| | June | 9.80 | $(4.55 \pm 0.24) \times 10^{-11}$ | 14 % | $(2.3 \pm 0.1) \times 10^{-10}$ | 3.9 ± 0.1 |
| | July | 3.27 | $(2.53 \pm 0.34) \times 10^{-11}$ | 8 % | $(1.7 \pm 0.2) \times 10^{-10}$ | 3.7 ± 0.2 |
| | August | 3.0 | $(4.50 \pm 0.45) \times 10^{-11}$ | 14 % | $(3.1 \pm 0.3) \times 10^{-10}$ | 3.9 ± 0.3 |

^aC.U. is the Crab Unit, as defined in the text.^bObservations performed with a single telescope, MAGIC-I and published in Aleksić et al. (2012).^cObservation was too short to allow for a reliable fit to the spectrum.

four and five. The flux varies from 4 to 18 percent C.U. across time. Finally, the last three columns list the results of the differential flux analysis, reporting the results of a fit with a simple power law function in the form

$$\frac{dF}{dE} = f_0 * \left(\frac{E}{200 \text{ GeV}} \right)^{-\Gamma} \quad (1)$$

where f_0 is the flux at 200 GeV (column six) and Γ is the power-law index (column seven in Table 1).

The overall emission above 150 GeV of PG 1553 + 113 observed with MAGIC from 2007 to 2017 is reported in Fig. 1. Data from 2007, 2008, and 2009 were collected with a single telescope and are from Aleksić et al. (2012). For the more recent data, a daily binning

was adopted. The 2010–2017 monthly averaged values are listed in Table 1, along with 2007–2009 yearly values from Aleksić et al. (2012). MAGIC started a regular monitoring of the source for seven months per year in 2015 (MJD ~57000). This explains the irregular and scarce sampling of the curve before 2015.

The daily flux above 150 GeV shows variations within a factor of ~10, and reached its maximum in 2012 during a historical flare reported in Aleksić et al. (2015). The average flux is $(2.74 \pm 0.04) \times 10^{-11} \text{ cm}^{-2} \text{ s}^{-1}$. The hypothesis of constant flux can be discarded, based on the χ^2 test for goodness of fit ($\chi^2/(\text{degrees of freedom}) = 1339/157$).

2.2 High energy gamma-ray data

Further gamma-ray data considered in the study are those collected with the *Fermi*-LAT and analysed above 100 MeV in Tavani et al.

Crab Nebula flux measured above the same threshold by MAGIC as reported in Aleksić et al. (2016b).

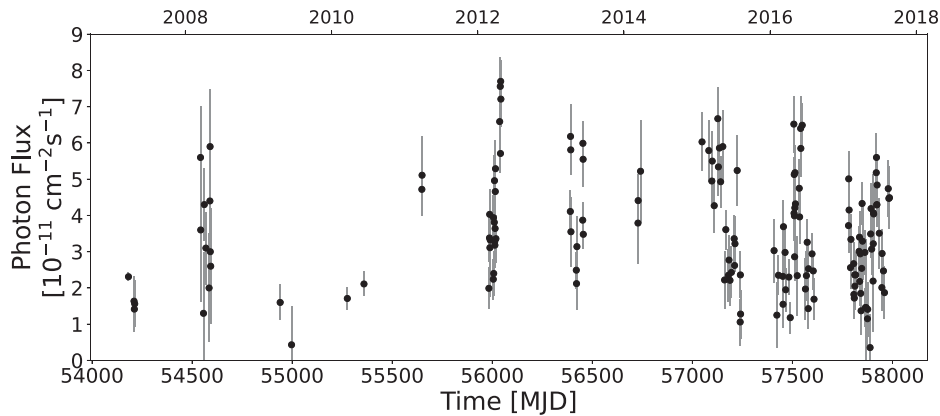


Figure 1. PG 1553 + 113 light curve above 150 GeV measured with the MAGIC telescopes.

(2018). In that work the authors added 2016 and 2017 data to the sample used in the original paper claiming the quasi-periodic behaviour (Ackermann et al. 2015). The *Fermi*-LAT data therefore cover almost continuously the 2008–2017 period and represent the only continuous monitoring considered. These data are analysed with 20 d binning.

2.3 X-ray data

The *Neil Gehrels Swift observatory* (*Swift*) (Gehrels et al. 2004) observed PG 1553+113 since 2005 during outbursts and almost regularly since 2013. We have collected all snapshots in the period from 2005 up to the end of 2017. PG 1553 + 113 was observed simultaneously with the X-ray Telescope (XRT; Burrows et al. 2005, 0.2–10.0 keV), and with all six filters of the Ultraviolet/Optical Telescope (UVOT; Roming et al. 2005, 170–600 nm). The *Swift*-XRT data, reported in Fig. 2, were collected in photon counting mode (PC) and windowed timing mode (WT). In both cases, the data were processed using the FTOOLS task `xrtpipeline` (version 0.13.5), which is distributed by HEASARC within the HEASoft package (v6.28). Events with grades 0–12 were selected for the data in PC mode, and with grades 0 – 2 for the data in WT mode. The corresponding response matrices available in the *Swift* CALDB version were used. When the source count rate in PC mode was higher than 0.6 counts s^{-1} the pile-up was evaluated following the standard procedure.² Observations affected by pile-up were corrected by masking the central 7 arcsec region. For each observation the extraction region was checked visually on the image and slightly centred to the peak of the signal, when needed. The signal was extracted within an annulus with an inner radius of 3 pixels (7 arcsec) and an outer radius of 30 pixels (70 arcsec). Events in different channels were grouped with the corresponding redistribution matrix (rmf), and ancillary (arf) files with the task `grppha`, setting a binning of at least 25 counts for each spectral channel in order to use the chi-squared statistics. The resulting spectra were analyzed with `Xspec` version 12.11.1. We fitted the spectrum with an absorbed power-law using the photoelectric absorption model `tbabs` (Wilms, Allen & McCray 2000), with a neutral hydrogen column density fixed to its Galactic value ($N_H = 3.67 \times 10^{20} \text{ cm}^{-2}$; Kalberla et al. 2005). The results are shown in Fig. 2.

²<http://www.swift.ac.uk/analysis/xrt/pileup.php>

2.4 UV data

Swift/UVOT data in the *v*, *b*, *u*, *w1*, *m2*, and *w2* filters are reported in Fig. 3 and were reduced with the HEASoft package v6.28 using the `uvotsource` task. We extracted the source counts from a circle with 5 arcsec radius centred on the source nominal position, corresponding to the optimal aperture on the source count rate (Poole et al. 2008). The background counts were extracted from a circle with 60 arcsec radius in a near, source-free region. Conversion of magnitudes into dereddened flux densities was obtained by adopting the extinction value $E(B-V) = 0.054$ as in Raiteri et al. (2015), the mean galactic extinction curve in Fitzpatrick (1999) and the magnitude-flux calibrations by Poole & Breeveld (2005). Statistical uncertainty on magnitudes of the order of 0.03 mag, on the zero-point UVOT calibration 0.02–0.06 mag (Poole, Breeveld & Landsman 2005) and the count ratio to flux correction (Poole & Breeveld 2005) have been propagated to estimate the error on the flux, resulting in a 4–6 per cent uncertainty.

2.5 Optical data

The optical *R*-band data were obtained as part of Tuorla blazar monitoring program.³ The observations are described in Nilsson et al. (2018). The data have been analysed using the semiautomatic pipeline for differential photometry developed at the Tuorla Observatory (Nilsson et al. 2018) using the comparison and control star magnitudes from Raiteri et al. (2015). The observed fluxes have been corrected for galactic extinction using a value of 0.113 from Schlafly & Finkbeiner (2011).

Other optical data were provided by the Whole Earth Blazar Telescope (WEBT) Collaboration.⁴ WEBT observations up to 2015 October were analysed in Raiteri et al. (2015, 2017a). New data in the 2016 and 2017 optical observing seasons were acquired at the following observatories: Abastumani (Georgia), Aoyama Gakuin (Japan), Crimean (Crimea⁵), Hans Haffner (Germany), Mt. Maidanak (Uzbekistan), Perkins (US), Rozhen (Bulgaria), Siding Spring (Australia), Siena (Italy), Sirio (Italy), St. Petersburg (Russia),

³<http://users.utu.fi/kani/1m> (Takalo et al. 2008).

⁴<https://www.oato.inaf.it/blazars/webt/> (Villata et al. 2002).

⁵In 1991, Ukraine with the Crimean peninsula became an independent state. While the Crimean Astrophysical Observatory became Ukrainian, the AZT-8 telescope located there continued to be operated jointly by the Crimean observatory and by the St. Petersburg group.

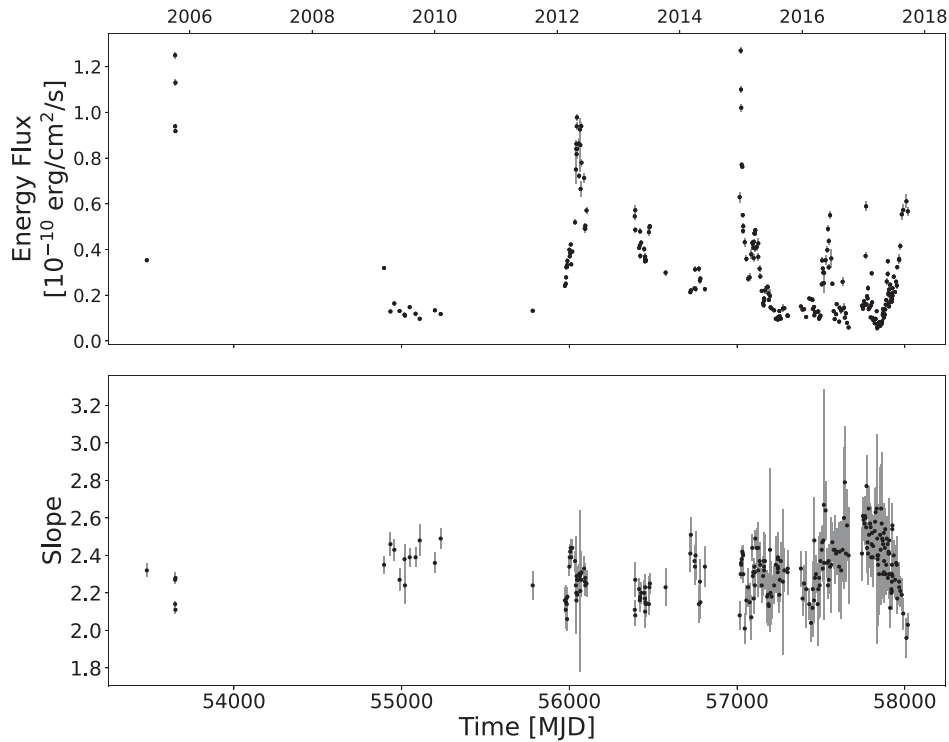


Figure 2. Top panel: PG 1553 + 113 light curve in the 0.5–10 keV band as detected with the *Swift*-XRT satellite. Bottom panel: spectral slope light curve resulting from an absorbed power-law fit.

Teide (Spain), Tjarafe (Spain), and at the Astronomical Station Vidojevica (Serbia). Additional WEBT observations were carried out with telescopes belonging to the Las Cumbres Observatory global telescope network at the Haleakala, Siding Spring, and Teide observing sites.

Calibration was performed using the same photometric sequence as in the case of KVA data. The *R*-band light curve obtained by assembling all data sets is shown in Fig. 3 and was carefully inspected and, when necessary, processed to obtain a homogeneous and reliable time series. Indeed, even if WEBT observers use the same photometric sequence, differences in equipment may lead to some offset between various data sets. These offsets clearly appear when data sets overlap in time and can consequently be corrected for. Moreover, we removed a few data points strongly deviating from the main trend traced by the bulk of the data sets, and mostly affected by large uncertainties. Finally, noisy intranight sequences from the same telescope were binned. The above processing is a necessary step to undertake if one wants to deal with light curves that can be used for robust analysis and modelling.

2.6 Optical polarization

We use optical polarization data obtained by the Nordic Optical Telescope (NOT), Liverpool Telescope (RINGO2), Skinakas Observatory (RoboPol), Crimean Astrophysical Observatory (AZT-8 + ST7 telescope and LX-200 telescope with SBIG ST7b), Perkins Telescope Observatory, and Steward Observatory. The NOT data reduction is described in Hovatta et al. (2016); MAGIC Collaboration et al. (2018). The RINGO2 data were obtained as a part of a

blazar monitoring programme at the Liverpool Telescope (Jermak et al. 2016) and the RoboPol data as a part of a blazar monitoring programme at the Skinakas Observatory (Blinov et al. 2021). The details of the data reduction of the AZT-8 + ST7 data are described in Larionov et al. (2008), and the Perkins telescope observations in Jorstad et al. (2010). The Steward Observatory data are publicly available and the polarimetric data are described in detail in Smith et al. (2009).

The data were obtained using the *R*-band filter except for the Steward Observatory where data were obtained using a filter between 5000 and 7000 Å. All data were checked for consistency and the polarization degree was corrected for positive bias using the formula in Wardle & Kronberg (1974). We removed six data points, which had a signal-to-noise ratio less than two in fractional polarization. In 2016, RoboPol observed the source with a faster cadence of multiple observations per night, and we averaged these to a single observation per night to avoid biasing our analysis with more densely sampled curves during that time.

In Fig. 3, we show the EVPAs starting from a range between 0° and 180°. The difference between the EVPAs of consecutive points is minimized to be less than 90° by adding or subtracting 180° from the following points. If the time gap between the points is longer than 50 d, we set the EVPA to the original range of 0°–180° as we do not know the evolution of the EVPA over such long gaps.

In all other cases, except for the Steward Observatory observations, photometry is also determined from the observations. The *R*-band magnitudes from these observations are also included in Fig. 3 along with the KVA and WEBT data. The polarization data are used in this paper for characterizing the general variability patterns, while more detailed physical modelling of the polarization is the subject of a separate paper (Nilsson et al. in preparation).

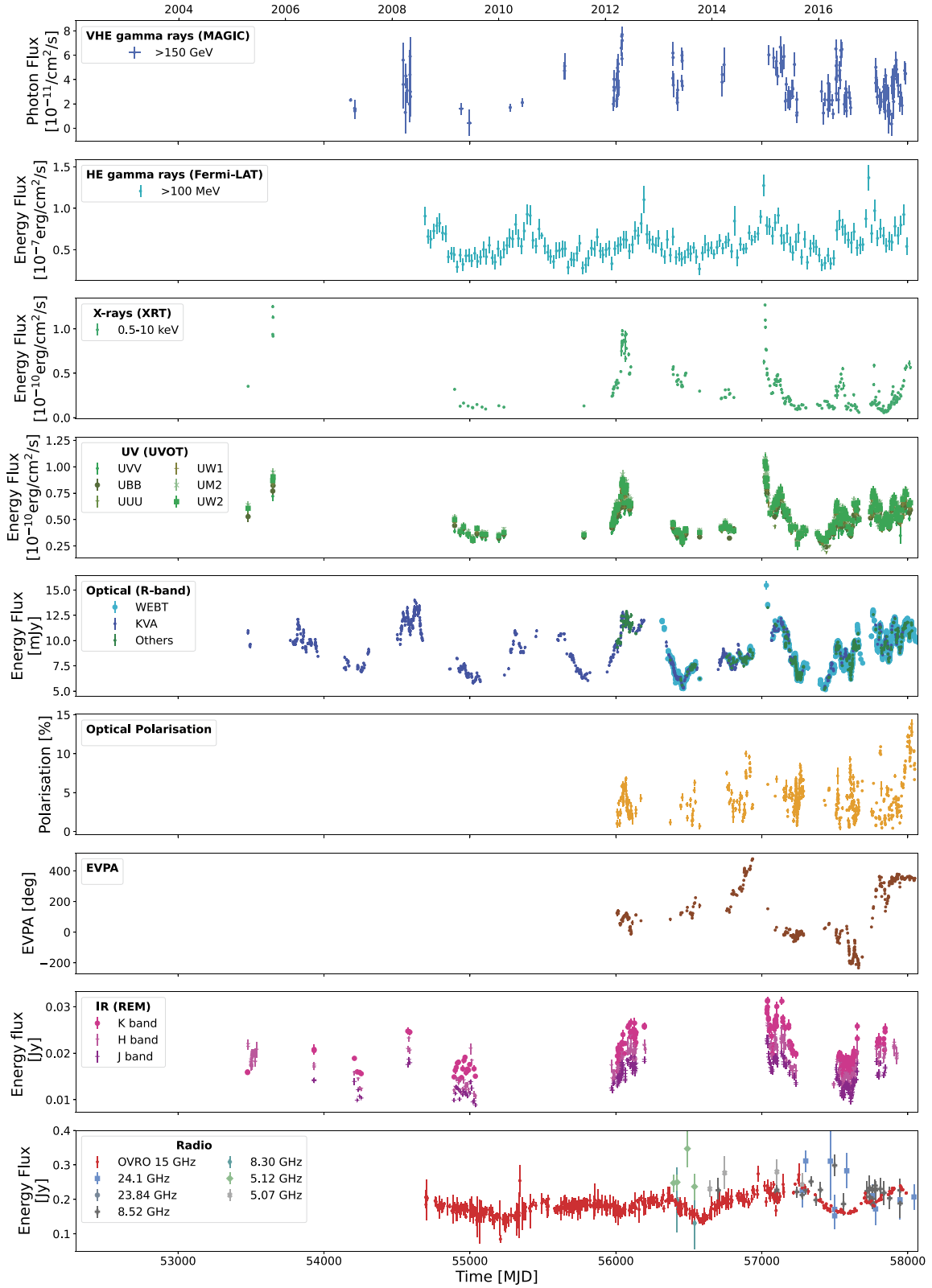


Figure 3. Long-term PG 1553 + 113 MWL light curves. From top to bottom: VHE gamma rays > 150 GeV (MAGIC, daily); HE gamma rays > 100 MeV (*Fermi*-LAT, 20 d binning, from Tavani et al. 2018); X-ray 0.5–10 keV (*Swift*-XRT); UV in six different filters (*Swift*-UVOT, same snapshots than *Swift*-XRT); optical in *R* band (WEFT, KVA, and from optical polarization telescopes labelled as ‘others’); Optical polarization and EVPA (NOT, RoboPol, Liverpool, Crimea, and Steward telescopes); Infrared in three different filters (REM); and Radio observations in seven different frequencies (OVRO and Medicina radio telescopes).

2.7 IR data

We observed PG 1553 + 113 with the Rapid Eye Mounting Telescope (REM, Zerbi et al. 2004), a robotic telescope located at La Silla Observatory (Chile). It performed photometric observations using NIR filters in the period from 2005 April 8 (MJD 53468) to 2017 June 20 (MJD 57802). REM data are shown in Fig. 3. The telescope is able to operate in a fully autonomous way (Covino et al. 2004), and data are reduced and analysed following standard procedures. Aperture photometry was derived using custom tools, and the calibration was based on the scheme described by Sandrinelli, Covino & Treves (2014).

We used reference stars from the *Two Micron All Sky Survey* (2MASS) *Catalog*⁶ (Skrutskie et al. 2006). All images have been visually checked, eliminating those where the targets or the reference stars are close to the borders of the frame, and where obvious biases were present.

2.8 Radio data

Regular 15 GHz observations of PG 1553 + 113 were carried out as part of a high-cadence gamma-ray blazar monitoring programme using the Owens Valley Radio Observatory (OVRO) 40 m telescope (Richards et al. 2011). PG 1553 + 113 was observed with a nominal twice-per-week cadence.

The OVRO 40 m uses off-axis dual-beam optics and a cryogenic receiver with a 3 GHz bandwidth centred at 15 GHz. The two sky beams are Dicke switched using the off-source beam as a reference, and the source is alternated between the two beams in an ON–ON fashion to remove atmospheric and ground contamination. In May 2014, a new dual-beam correlation receiver was installed on the 40 m telescope and the fast gain variations are corrected using a 180 degree phase switch instead of a Dicke switch. The performance of the new receiver is very similar to the old one and no discontinuity is seen in the light curves (see Fig. 3). Flux density calibration is achieved using a temperature-stable diode noise source to remove receiver gain drifts and the flux density scale is derived from observations of 3C 286 assuming the Baars et al. (1977) value of 3.44 Jy at 15.0 GHz. The systematic uncertainty of about 5 per cent in the flux density scale is not included in the error bars. Complete details of the reduction and calibration procedure are found in Richards et al. (2011).

Radio observations were also carried out with the 32-m dishes located in Medicina (at 8 and 24 GHz) and Noto (at 5 GHz). Continuum acquisitions were performed exploiting On-The-Fly cross-scans in Equatorial coordinates. Flux density calibration was carried out observing 3C 286, 3C 123, NGC 7027 and, prior to 2018 January, also 3C 48. Reference flux densities for the calibrator sources were computed for the observed band central frequency, according to Perley & Butler (2013). For 24-GHz observations, the atmospheric contribution was also taken into account in the calibration procedure; the zenith opacity was estimated by means of skydip acquisitions. The data reduction was performed using the Cross-Scan Analysis Pipeline described in Giroletti & Righini (2020).

3 CHARACTERIZATION OF THE VARIABILITY

Fig. 3 displays the light curves collected from PG 1553 + 113 at several wavelengths from radio (bottom panel) to VHE gamma-rays

(top panel), for 12 yr, from 2005 to 2017 as described in the previous section.

A large part of the HE gamma-ray data data set, as well as radio and optical data sets, are published in Abramowski et al. (2015) and were used for the periodicity analysis.

The only instrument considered in this work that performed a continuous monitoring is *Fermi*-LAT. Also radio data have very good coverage, followed by optical data that suffered only from a few months break per year related to the visibility of the source. The coverage is more scattered for IR, UV, X-rays, and VHE gamma-ray data that are strongly affected by sparse sampling and often the observations are driven by a high state alert trigger, and therefore may be biased towards high states. In these bands, the coverage had a clear improvement starting from late 2014 (MJD \sim 57000). This is the result of an intense MWL and multiyear campaign aimed at a precise monitoring of the source state for the detailed modelling of the source emission and periodicity.

From a visual inspection of Fig. 3 we can conclude that the source shows high variability over the years in all bands, with moderate variations in radio and more pronounced variations in the other bands. This behaviour is quite common in HBLs (Acciari et al. 2021).

A detailed characterization of the variability is the key to investigate the physical phenomenology responsible for the broad-band emission as detailed in Rieger (2019) and references therein. In the following subsections, several variability studies are presented. The aim is two-fold: first, the characterization of the variability (and periodicity) at different bands. Secondly, the identification of interband connections. These connections are a powerful tool to unveil single/multiple regions responsible for the observed emission.

3.1 Flux-spectral index correlation

A clear correlation between the integral flux and the slope of the power law approximating the differential energy flux in X-rays and gamma rays characterises many flaring events of BL Lacs. In the case of negative correlation, the effect is often referred as harder-when-brighter behaviour (see e.g. Albert et al. 2007). This behaviour is associated with a shift of the synchrotron peak during flares, meaning that more energetic electrons are responsible for the bulk of the emission (see e.g. Acciari et al. 2021).

A study of the flux-slope correlation was performed for the VHE gamma-ray and X-ray data. The results are shown in Fig. 4. The monthly averaged MAGIC data from 2010 to 2017 were considered for the study. No correlation appears in the MAGIC data, but the large time interval considered and the relatively low statistics involved in the study may have diluted this correlation. X-ray data show instead a hint of anticorrelation between the spectral index and the flux state, indicating a harder-when-brighter trend. To evaluate the level of correlation we adopted the Spearman correlation coefficient, a value close to (-1) pointing to a strong (anti-)correlation. The Spearman correlation coefficient in X-ray data is -0.39 , and the p -value of the null-hypothesis (i.e. no-correlation) is $\sim 10^{-10}$.

It is important to emphasize that, contrary to the vast majority of studies available in literature claiming a harder-when-brighter trend in the considered bands (e.g. Pian et al. 1998; Albert et al. 2007; Acciari et al. 2020), the results presented here are not from a single campaign/flare, but they come from a large time interval spanning more than 10 yr.

⁶<http://www.ipac.caltech.edu/2mass/>

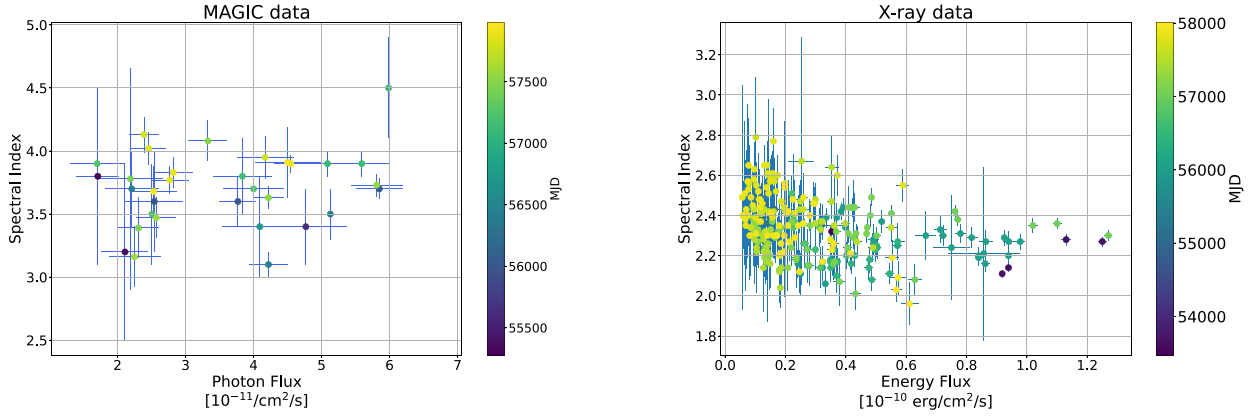


Figure 4. Correlation study between the flux level and the spectral index of the power-law fit to the data above 150 GeV (left, MAGIC monthly averaged) and in the 0.5–10 keV band (right, *Swift*-XRT individual pointing).

3.2 Variability time-scale

Apart from few exceptions (e.g. Acciari et al. 2020), blazars are highly variable objects in almost all bands. In HBLs, the variability time-scale may range from months down to a minute time-scale. According to special relativity, the comoving size of the emitting region, $\Delta r'$, can be constrained by the variability time-scale, (as detailed in Rieger 2019). The variability time-scale pinpoints the properties of the region responsible for the observed radiation. Interestingly, subday variations represent a challenge for the simplest emission models in blazars (e.g. Tavecchio, Maraschi & Ghisellini 1998), and for the subclass of Flat Spectrum Radio Quasars (e.g. fast variability – 10 min doubling time –observed in VHE gamma rays in PKS 1222 + 21, Aleksić et al. 2011).

To constrain the variability time-scale of PG 1553 + 113, a search for intraday variations was performed on MAGIC and *Swift*-XRT data. For statistical reasons, the study was limited to 10 snapshots with the highest flux recorded in both bands. The average duration of MAGIC observations was 1 h, while the average duration of *Swift*-XRT observations was 1.2 ks. The analyses revealed no hint of intraday variability in *Swift*-XRT and MAGIC data.

3.3 Interband correlation

Short or long-term correlation between the fluxes emitted at different bands allows us to track down the connection between photons emitted at different possible regions in the jet or with different, but correlated, mechanisms. This is the case of synchrotron self-Compton emission (SSC), where low-energy synchrotron photons are emitted together with inverse Compton, high-energy photons produced by the same electrons upscattering the synchrotron photons.

In our study, we focus on the interband correlation search on the IR, optical, UV, X-ray, HE and VHE gamma-ray bands. Radio data are excluded from this study in consideration of the well known lag due to the different location of the emission zone, that will be further discussed in the text.

The results of the correlation analysis performed with the Spearman test as implemented in the *SciPy* python package are listed in Table 2, where the Spearman coefficient and the p -value appear in the third and fourth columns, respectively.

For this study, only data within a 1.5-d window have been considered simultaneous apart for the correlation studies involving *Fermi*-LAT data where the simultaneity window has been extended to ± 10 d, to have sufficient statistics and in agreement with the

Table 2. Results of the correlation study between integral flux in different bands ordered by decreasing Spearman coefficient (third column). The simultaneity window assumed is ± 1.5 d apart for the correlation studies involving *Fermi*-LAT data, where it has been extended to ± 10 d. The last two columns report the p -value (null hypothesis: no correlation with close to zero time lag) and, if available, the panel with the scatter plot in Fig. 5, respectively.

| Band-1 | Band-2 | Spearman Coeff. | p -value | Panel |
|------------------|-------------------|-----------------|------------|-------|
| Optical | UV | 0.94 | 4e–88 | a |
| Optical | IR | 0.90 | 2e–50 | b |
| UV | HE γ -ray | 0.66 | 3e–10 | |
| Optical | HE γ -ray | 0.63 | 2e–14 | c |
| UV | VHE γ -ray | 0.62 | 9e–08 | |
| IR | HE γ -ray | 0.61 | 1e–05 | |
| X-ray | VHE γ -ray | 0.60 | 6e–08 | d |
| IR | UV | 0.60 | 4e–06 | |
| UV | X-ray | 0.55 | 6e–18 | e |
| Optical | X-ray | 0.37 | 4e–08 | f |
| HE γ -ray | VHE γ -ray | 0.39 | 0.006 | g |
| Optical | VHE γ -ray | 0.35 | 2e–05 | h |
| X-ray | HE γ -ray | 0.32 | 0.006 | i |
| IR | VHE γ -ray | 0.26 | 0.09 | |
| IR | X-ray | 0.29 | 0.02 | |

Fermi-LAT data binning of 20 d. The Table is ordered by decreasing the correlation levels according to this indicator. Similar results are obtained with the weighted Pearson's coefficient (that has the advantage of taking into account the errors of the flux, but the disadvantage of assuming a Gaussian distribution of values). Fig. 5 and 6 show some selected scatter plots, also indicated in the last column of Table 2.

The main results of the correlation analysis are as follows:

- (i) A strong correlation (Spearman coefficient ≥ 0.9) is observed both between optical and UV (UW2 band) and optical and IR (H band) data;
- (ii) Optical and UV data show a net correlation (Spearman coefficient ≥ 0.6) also with the HE gamma ray data. A similar relation is also observed between X-rays and VHE gamma-rays;
- (iii) X-ray and UV data, with strictly simultaneous sampling, show a milder correlation (Spearman coefficient = 0.55);

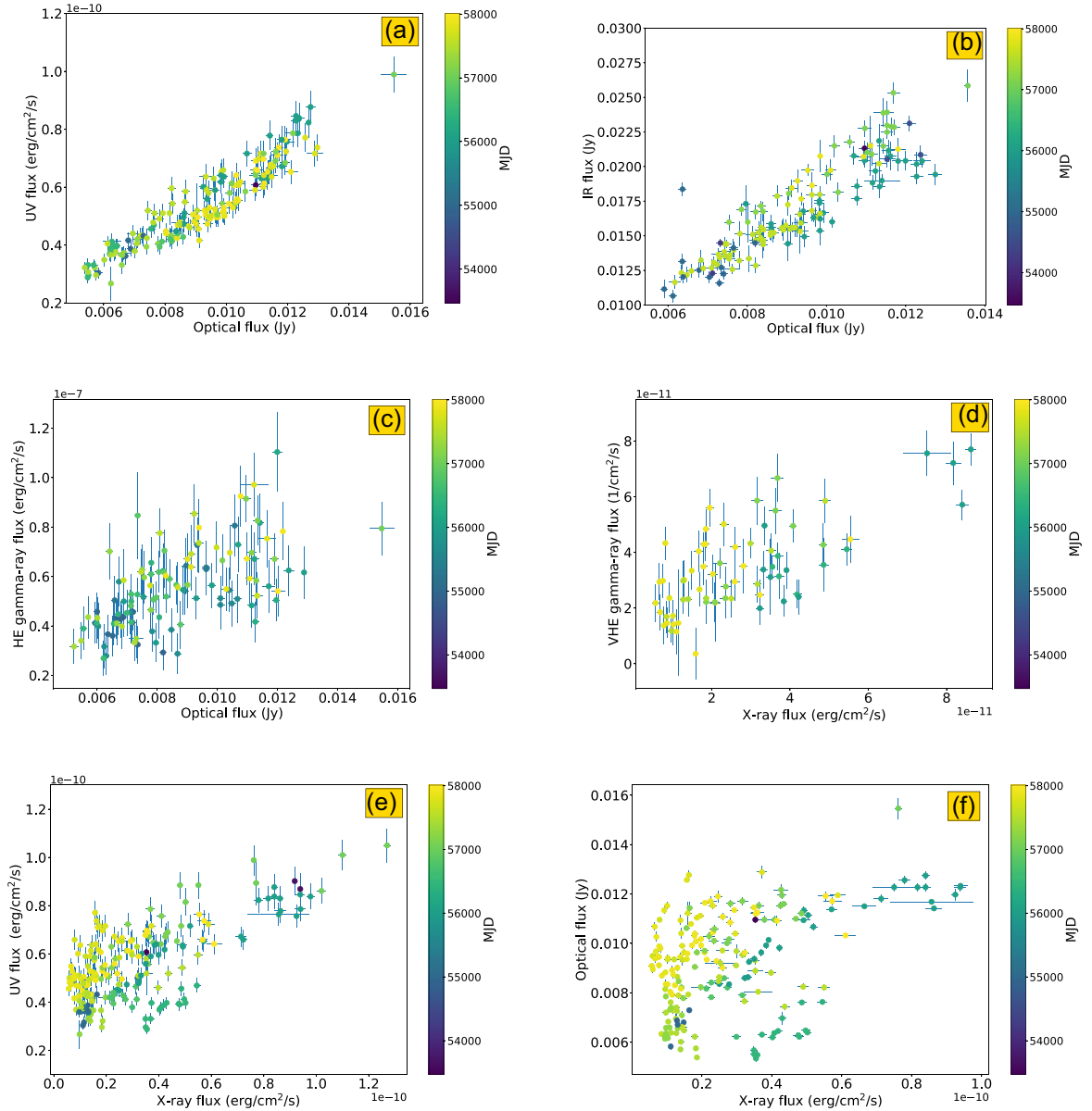


Figure 5. Selected scatter plots used to investigate flux correlations. For correlation studies involving *Fermi*-LAT, the simultaneity window has been set to ± 10 d. In all other cases, the window assumed for simultaneity is ± 1.5 d.

(iv) Only a hint of correlation (Spearman coefficient ≤ 0.4) with close to zero time lag is observed between the other bands (HE and VHE gamma rays, optical/X-ray, and optical VHE gamma rays).

(v) In the optical/X-ray case, a careful analysis of the scatter plot allows us to identify episodes with different correlation behaviours: from a clear correlation, corresponding to the X-ray and optical flare at MJD ~ 57000 to anticorrelated events (X-ray enhanced state at MJD ~ 57500), as highlighted in Fig. 7.

These results suggest a common origin for the spectral features observed in IR, optical, UV, and *Fermi*-LAT bands. In particular, IR, optical, and UV photons are likely synchrotron photons from the same emitting region. Single-zone SSC process is the cogent mechanism connecting optical and HE gamma-ray photons. The same process may be responsible for the X-ray to VHE gamma-ray connection, even if the radiation should come at least in part

from a different (or additional) region with respect to the low-energy counterpart, to explain the weaker correlation with the other bands.

The possibility of a delay in the PG 1553 + 113 correlation between bands has recently been investigated in Liodakis et al. (2018) for the radio, optical, and gamma-ray bands. Although gamma-ray and optical data are consistent with no time-lag correlation, a delay of ~ 3 –4 months appears between radio and both optical and *Fermi*-LAT data. We have investigated the possibility of a delay between radio and X-ray and VHE gamma-ray data, between *Fermi*-LAT and X-ray and VHE gamma-ray data, and between X-rays and VHE gamma rays with the same method presented in Liodakis et al. (2018). In all cases, from the discrete correlation function study no significant time lag emerged. The analysis of radio and optical/gamma-ray data, instead, are fully consistent with those reported in Liodakis et al. (2018). A delayed correlation in the radio band is well-known effect in blazars and is due to the

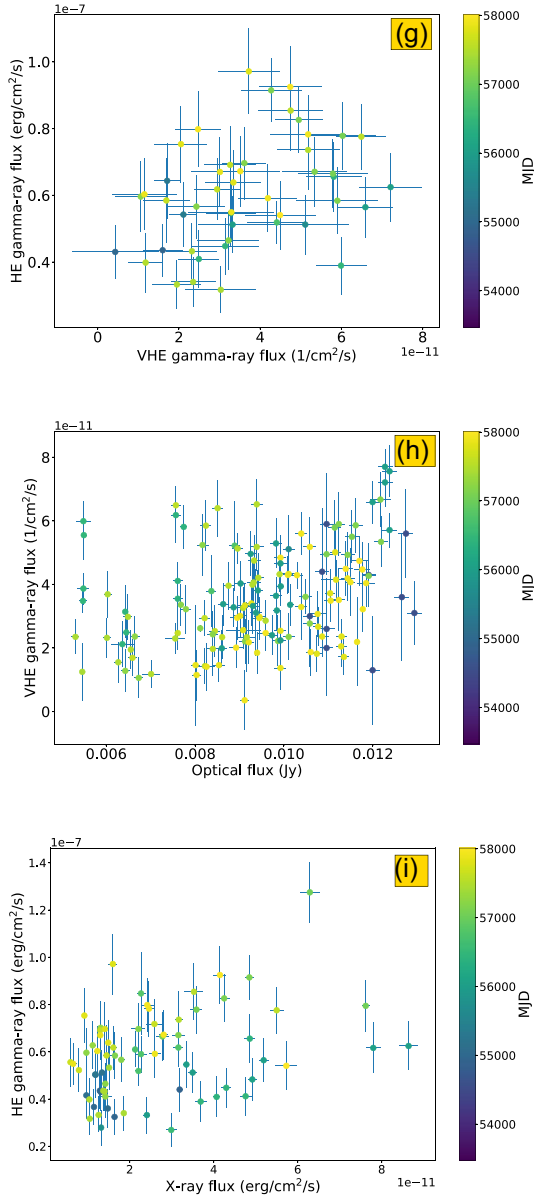


Figure 6. Continue from Fig. 5.

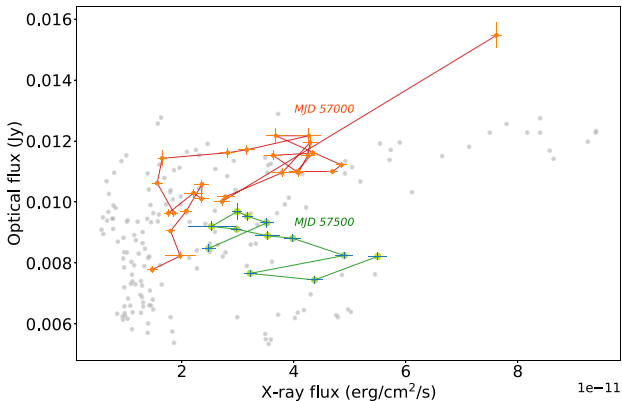


Figure 7. Two selected episodes with different correlation behaviour, correlation (MJD 57000) and anticorrelation (MJD 57500), in the optical-X-ray scatter plot.

self-absorption of radio emission, which becomes visible when the density of the region drops, inducing a delay with respect to high-energy emission.

3.4 Bayesian block analysis

In order to determine variations and flares in the MWL light curves, we model flux variations in a model-independent manner using Bayesian blocks (Scargle et al. 2013). Fig. 8 shows the Bayesian block representation of the MWL light curves, including the optical polarization degree. We have optimized the prior of the slope on the number of bins for individual light curves to better match their sampling and variability.

We find interesting flaring behaviour across all wavelengths. For example, we find contemporaneous flares in X-rays, UV, optical, and elevated activity in VHE gamma rays and polarization at ~ 56060 MJD that does not seem to have a counterpart in the *Fermi*-LAT band. On the other hand, we find contemporaneous flares in optical, UV, X-rays and gamma-rays at ~ 57020 MJD. The 15 GHz radio also seems to be in an elevated state during that time, although the radio light curve does not follow the variability patterns in other wavelengths. Unfortunately, apart from ~ 57020 MJD, the prominent *Fermi* flares fall into optical and/or VHE gamma-ray gaps, although in all of them the optical seems to be in an elevated state.

4 PERIODIC MODULATION IN THE MWL LIGHT CURVE

As first proposed in Ackermann et al. (2015) and then confirmed in several other studies (Gupta et al. 2016; Prokhorov & Moraghan 2017; Sandrinelli et al. 2018; Covino et al. 2020), a periodic modulation of the HE gamma-ray emission is firmly established in *Fermi*-LAT data. Although the optical curve appears to be much more complex than *Fermi*-LAT curve, the modulation with a period similar to that observed at higher frequencies is found, with a smaller significance (Tavani et al. 2018).

As a first step in the periodicity study, we visually inspected if the light curves at different bands are in agreement with the hypothesis of a periodic modulation of period $P_{\text{fermi}} = 798$ d. To this purpose, we built a normalized MWL folded light curve assuming a period of 798 d (Ackermann et al. 2015). The final result is shown in Fig. 9 obtained for all data reported in Fig. 3 for the radio, optical polarization, optical, UV, X-ray, HE gamma-ray, and VHE gamma-ray bands. In each bin, the average value and its error are reported with a continuous line. The bars instead represent the square root of the variance of the folded data of each phase bin. We underline that, while the error on the average is strongly dependent on the number of points in that bin, the variance is not. Therefore, the latter is an indication of the dispersion of the sample, except for a few cases with bins with a single point (hence with a low uncertainty that is by no means representative of the real dispersion).

As expected, the HE gamma-ray folded curve displays a clear peak at phase ~ 0 . The minimum emission is instead located at phase 0.3–0.5. The same trend is observed in the optical and UV curves, while the radio curve behaviour seems shifted, in agreement with the delayed emission resulting from the DCF analysis in Liodakis et al. (2018), also confirmed in our study.

It is interesting to note that, despite the poor sampling of the light curves, X-ray, and VHE gamma ray-folded curves are almost fully characterized, meaning that the observations carried out in the

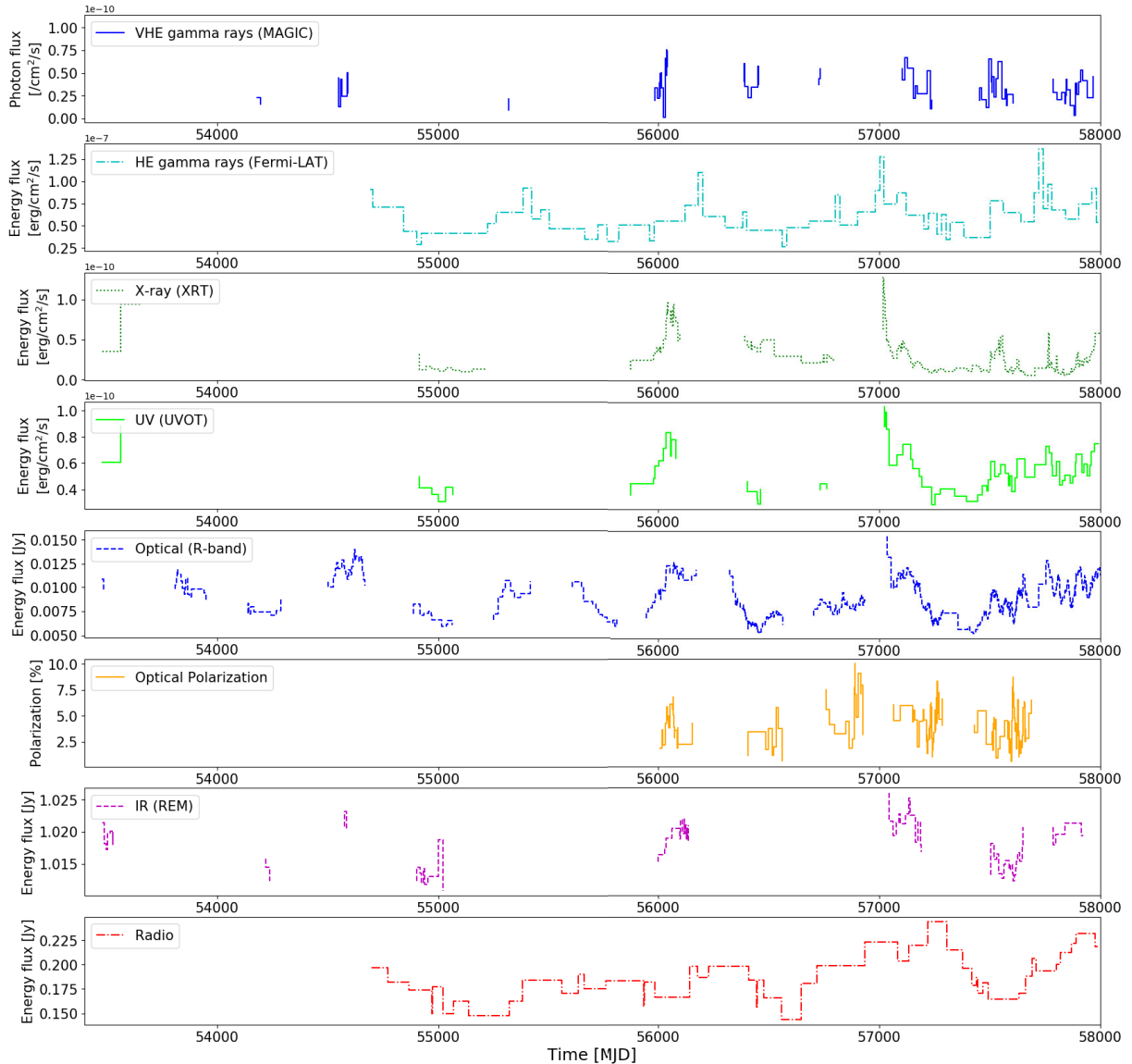


Figure 8. Bayesian block representation of the MWL light curves having excluded the observational gaps.

11 yr considered were diluted in different phases of the assumed periodic modulation. This allows us a first qualitative study of the trend of these curves. The main finding of this study is that while the folded curves, including the optical polarization, show a minimum in the phase interval 0.3–0.5, in agreement with the observations in the HE gamma-ray band, no clear maximum is observed in the optical polarization, X-ray, and VHE gamma-ray bands.

In parallel with this visual inspection, we have also carried out a study of periodicity, which is reported in the next section.

4.1 Systematic search for periodicity

In all bands we search for a sinusoidal periodic signal using the Generalized Lomb–Scargle (GLS) periodogram (Zechmeister & Kürster 2009) as implemented in the PyAstronomy python package⁷

⁷<https://github.com/sczesla/PyAstronomy>

(Czesla et al. 2019) with frequencies ranging from $1/T$ to $N/(2T)$ sampled in steps of $1/(10T)$, where T is the total time of the light curve and N is the number of data points.

We identify the period and power of the strongest peak. In the periodogram of the radio data the GLS power at the lowest frequency is higher than the next strongest peak; however, we do not take the low-frequency peak into consideration because the peak period lies outside of the covered frequency range and less than one full cycle would be covered by the full data.

We need to assess whether a detected peak provides significant evidence for an intrinsic periodicity or whether it is a sporadic result of the typical flaring behaviour. We follow the procedure described in appendix A of O’Neill et al. (2022). Our Null hypothesis is that the light curves follow a stochastic red-noise process, with the same statistical properties of the original data – namely the power spectral density (PSD) and probability density function (PDF). We assume a power-law PSD $\sim \nu^{-\beta}$, where ν is the frequency, and estimate the index, β , with an implementation of the method introduced by Uttley, McHardy & Papadakis (2002). In the radio band the index

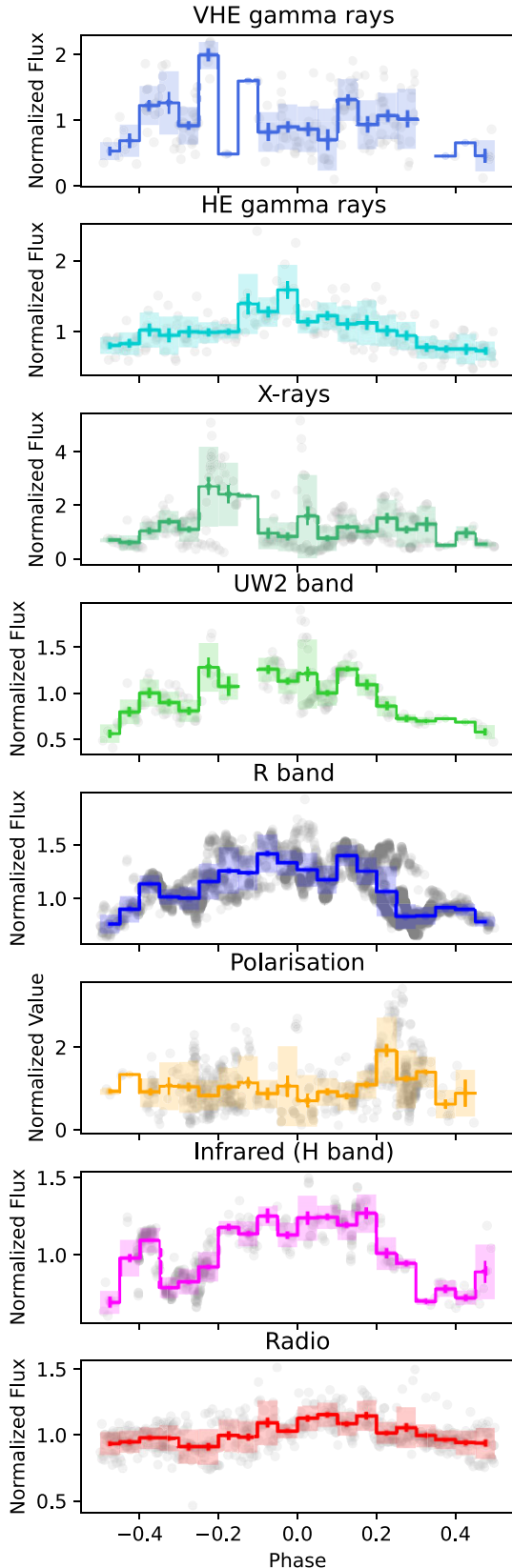


Figure 9. PG 1553 + 113 MWL folded light curves obtained by assuming a period of 798 d. In each panel, the average values are reported with a continuous line. The error bar in each bin is the standard error of the mean values. The coloured bar in each bin represents the variance of the data distribution.

was found to be 2.0 ± 0.51 and for the MAGIC data 1.0 ± 0.42 , for the remaining bands ranging from 1.4–1.5 with uncertainties ranging from 0.1 to 0.26.

We estimated the PDFs through the empirical cumulative distribution functions (ECDFs) of the light curves. For the *Fermi*-LAT analysis we created 50 000 simulations, for all other bands 10 000 simulations each, that implement the Null hypothesis. We calculate the GLS for all simulations and count the simulations that have a power equal to or higher than the peak power at the peak frequency of the data GLS; this gives us the local p -value, i.e. the probability that a red-noise process results in an apparent periodicity as strong or stronger than observed at specifically the frequency where it was detected. The local p -value does not take into account that we test many frequencies. To take the look-elsewhere-effect into account we identify the strongest peak (discarding peaks at the edge of the frequency range) in the GLS of each simulation and calculate its local p -value, then we count all simulations with peaks that have a local p -value equal to or lower than the local p -value of the data GLS peak to estimate the global p -value.

Our results are reported in Table 3, where the PSD index, the peak period in days, the peak power and the local and global p -values are listed as a function of the considered band (first column). The GLS of the *Fermi*-LAT light curve shows a prominent peak at a period of 786 d, with a global p -value of 1.0×10^{-3} , which corresponds to 3.1σ in a one-sided test if the statistic were normal distributed. At an a priori chosen significance level of 3σ we reject the Null hypothesis that the detected peak in the periodogram is a likely result of a red-noise process and conclude that light curve very likely contains a truly periodic signal.

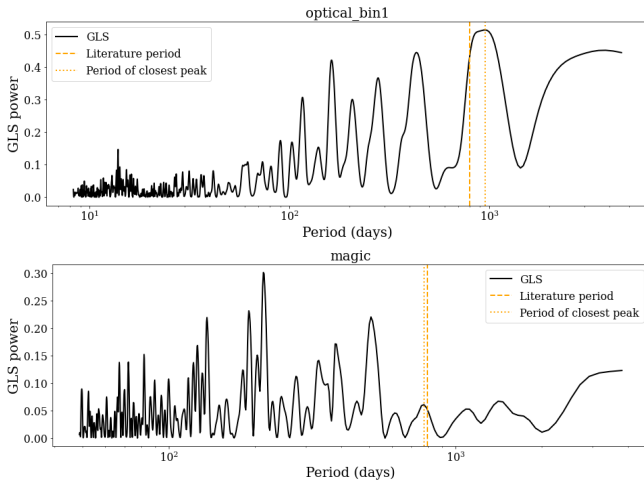
The *Swift*-XRT and MAGIC data do not show evidence for a significant periodicity, as the p -values suggest that the data behaviour is fully consistent with the null hypothesis. The *Swift*-UVOT and radio light curves show the strongest GLS peaks at periods at 806 and 865 d, but cannot be considered significant with global p -values as high as 10 and 3 per cent.

Before the analysis of the optical light curve, including all the optical data collected in the campaign, we averaged data points within time ranges of 1 d weighted by the corresponding uncertainties. In the GLS of the optical light curve we identify the strongest peak at a period of 957 d with a local p -value of ~ 10 per cent and a global p -value of 47 per cent. This result appears to be in conflict with those of Sandrinelli et al. (2018), who claim a period of 810 ± 52 d with p -values of 1 or 5 per cent depending on the method used, and the results of Agarwal et al. (2021), who found periods in the range of 801–812 d with uncertainties ranging from 20 to 70 d, depending on the analysis method and specific band (V or R) with a p -value < 1 per cent. However, we find that the strongest GLS peak, shown in Fig. 10 (upper panel) shows a broad, flat plateau covering the period range from ~ 800 to 1000 d. Therefore, the period is poorly constrained. Furthermore, the local p -value strongly depends on the period in that period range. Towards shorter periods the local p -value decreases and is ~ 5 per cent at a period of ~ 800 d, comparable to one of the results of Sandrinelli et al. (2018). Regarding the optical data we currently do not find convincing evidence for a true periodicity and we conclude that if there truly is a periodicity in the light curve more cycles need to be covered by observations to get a better constraint on the period and the significance.

To complete our analysis, we have estimated the local p -value in the above-mentioned GLS at the literature period of 798 d (Ackermann et al. 2015). This approach, also in line with the folded light curve presented in the previous Section, has the advantage of minimizing the trial factors, since only a single period is tested. The

Table 3. Results of the search for periodicity in the different bands.

| Band | PSD index | Peak period [d] | Peak power | Local p -value | Global p -value | p -value (lit. period) |
|--------------------|-----------------|--------------------|------------|----------------------|----------------------|-----------------------------|
| Radio 15 GHz | 2.0 ± 0.51 | 865 | 0.40 | 2.3×10^{-3} | 3.4×10^{-2} | 2.0×10^{-2} |
| Optical | 1.47 ± 0.08 | 957 | 0.51 | 9.7×10^{-2} | 4.7×10^{-1} | 7.8×10^{-2} |
| <i>Swift</i> -UVOT | 1.41 ± 0.12 | 806 | 0.46 | 5.6×10^{-3} | 1.0×10^{-1} | 5.6×10^{-3} |
| <i>Swift</i> -XRT | 1.5 ± 0.10 | 2521 | 0.47 | 1.4×10^{-1} | 6.8×10^{-1} | 8.6×10^{-1} |
| <i>Fermi</i> -LAT | 1.4 ± 0.26 | 786 | 0.40 | 2.0×10^{-5} | 1.0×10^{-3} | 2.0×10^{-5} |
| MAGIC | 1.0 ± 0.42 | 214 | 0.30 | 1.8×10^{-2} | 3.7×10^{-1} | 7.0×10^{-1} |


Figure 10. GLS periodogram of the optical (upper panel) and MAGIC (lower panel) data. The optical data show a broad GLS peak, described in the text. In case of MAGIC data, no significant peak emerged from the study.

resulting p -values are listed in the last column of Table 3. The *Fermi*-LAT p -value reflects the local p -value, which is expected as it is the period determined by a subsample of the same data. The radio, optical, *Swift*-UVOT p -values decrease to 2, 7.8, and 0.56 per cent, respectively, while the p -values in case of MAGIC and *Swift*-XRT data are well compatible with the null hypothesis with values 70 and 86 per cent, respectively. The optical and MAGIC GLS are displayed in Fig. 10.

4.2 Further search for periodicity

A significant indication of periodicity in the gamma-ray light curve measured by *Fermi*-LAT was found in several other studies. Among those, the work by Peñil et al. (2020) implemented different methods to detect periodicity in *Fermi*-LAT blazars. We used the same pipeline described in Peñil et al. (2020), focussing on the Lomb–Scargle and on the wavelet transform approaches, and extending it to the search for periodicity to the VHE, X-ray, UV and optical bands. The details on the two methods can be found in the corresponding paper. The results on the *Fermi*-LAT light curve is reproduced providing a peak at the period of ~ 800 d with a p -value $< 1 \times 10^{-4}$ (pre-trial). The significance of the periodicity was evaluated with respect to the null hypothesis of a stochastic red noise with the same statistical properties of the light curve of the original data. Similar period and significance are obtained on the optical light curve, in contrast to the analysis described in the previous section, but slightly compatible with the works (Ackermann et al. 2015; Covino et al. 2020; Peñil

et al. 2020). As it was commented previously, this can depend on the broad and flat peak in the GLS; any further assessment on the periodicity on the optical band will require further observations. The analysis on the X-ray and VHE data confirms the previous findings, showing no significant periodicity (p -value of > 0.1) at the highest peak.

5 DISCUSSION AND CONCLUSIONS

We have analysed the MWL behaviour of PG 1553 + 113 using MAGIC and MWL data from 2007 until the end of 2017 covering bands from radio to VHE gamma rays. The main motivation of this work was to study if the 2.2-yr periodicity seen in the GeV gamma rays by the *Fermi*-LAT (Ackermann et al. 2015) can be seen in our MAGIC data, and if the MWL data can be used to constrain the models explaining the periodicity.

For these purposes, we have first characterized the variability in the VHE gamma-ray and X-ray bands. In both cases, we have not found evidence of intraday variability. Interestingly, intraday variability in the X-ray band was detected by Raiteri et al. (2017a) in long *XMM-Newton* observations performed in 2015. From the ~ 1 h variability time-scale, they inferred a size of the emitting region $R \lesssim 8 \times 10^{14}$ cm. Recently, Dhiman et al. (2021) confirmed the intraday variability of PG 1553 + 113 in the 0.3–10 keV band with *XMM-Newton* data taken during 2010–2018. The authors found an indication of variability in 16 over 19 observations, where the duration of the observations ranged from 21 to 140 ks. The doubling time-scale ranged from 2 to 33 ks, i.e. ~ 30 min to ~ 9 h. The short duration of our single pointings prevented us to probe intranight variability in $>$ hour time-scales, as the one suggested in Dhiman et al. (2021) study.

X-ray data in our sample show a hint of harder-when-brighter behaviour often detected in blazars (even if usually it is observed over a shorter time-scale). This indicates that possibly freshly injected, high-energy electrons are responsible for the X-ray variability. Furthermore, the long time span considered ensures that the mechanisms driving the spectral variability did not change substantially over time. The same study applied to the MAGIC data gave inconclusive results, probably due to the 1-month averaging applied to the data. A detailed spectral study is planned in a future publication and is beyond the scope of this work.

Interband correlation studies performed on IR, optical, UV, X-ray, HE, and VHE gamma-ray data confirmed the strong IR/optical/UV connection, related to the common synchrotron origin of the emission. An evident correlation between X-rays and VHE gamma rays, and between optical/UV/IR and HE gamma-ray, also emerged from this study, suggesting intertwined emission processes such as that foreseen in the multizone, SSC emission scenario.

Another piece of the puzzle is represented by the detected delayed correlation (of about 3–4 months) between the radio and both optical and *Fermi*-LAT emission (Liodakis et al. 2018). This result is in line with the average behaviour found in gamma-ray detected blazars reported in the same paper. Interestingly, this time-delayed correlation is not present in our radio and X-/VHE gamma-ray data.

After this detailed characterization of the variability in general, we have focused on the study of the periodicity.

A search for evidence of periodicity in the X-ray and TeV bands, as well as in the optical, UV, and GeV bands was performed with a solid statistical approach.

Our main finding of the periodicity analysis with the GLS method was that the X-ray and VHE gamma-ray data do not show statistical evidence for a periodic signal. Remarkably, a (hint of a) periodic signal compatible with the one published in literature was found only in the gamma-ray data, which is also the only band with a continuous coverage. A solid statistical analysis was applied to the data in the other bands. Radio, UV, and optical data show a periodogram with a peak compatible with the one firmly established in *Fermi*-LAT observations, but with a relatively high p -value (ranging from 4 to ~ 50 per cent). This is in agreement with the folded MWL light curve built assuming the literature period. The visual inspection of the MWL folded light curve suggests a hint of periodic behaviour in the radio, optical, UV, and HE gamma-ray bands. The peak is more pronounced in gamma rays and radio, while it appears broader, and with a similar pattern, in the R and UV2 bands. Polarimetric data, as well as X-ray and VHE gamma-ray data do not show any evident peak in the periodogram. X-ray and VHE gamma-ray folded curves exhibit a similar pattern. Interestingly, a low activity was recorded in all bands at approximately the same phase.

The observed periodicity may be interpreted as a periodic perturbation of the accretion rate on the SMBH and consequently of the fuelling at the base of the jet. The presence of a secondary black hole in a sub-parsec orbit with respect to the primary SMBH originating the jet represents a natural explanation, as previously invoked for OJ 287, despite not unique (e.g. Dey et al. 2018). Different mechanisms such as jet precession, internal jet rotation, or helical jet motion may also be invoked to explain the periodicity.

The most direct way to constrain a simple precessing jet model would be to observe motion of the jet on the sky. This has been studied in the radio band by Caproni et al. (2017) who modelled 15 GHz VLBA data of PG 1553+113 taken between 2009 and 2016 using a precessing jet model. They modelled the jet using individual Gaussian components, which they then connected to episodes of gamma-ray flares. More recently, the radio jet properties of PG 1553 + 113 were studied by Lico et al. (2020) using VLBA observations taken between 2015–2017 and light curves from OVRO between 2008–2018. While they found clear enhanced activity periods in the radio data, they were not found to be correlated with the 2.2-yr gamma-ray periodicity. Moreover, they concluded that the position angle variations of the jet of PG 1553 + 113 were not correlated with the gamma-ray periodicity, and a simple geometric model where the variability is caused by changes in the Doppler boosting cannot explain the periodicity, if the gamma-ray and radio variations originate in the same region of the jet.

Lico et al. (2020) also studied the radio polarization of PG 1553+113 using their VLBA data. They found that periods of enhanced polarization were connected with total intensity flares, indicating that the mechanism producing them is connected. Additionally, they saw a flattening of the radio spectral index at the times of total intensity activity. Such a behaviour could be expected, for example, when shocks compress magnetic field lines,

which both increases the fractional polarization and induces particle acceleration, which flattens the spectral index and increases the total intensity. They also suggested that the low polarization observed in the core region of PG 1553 + 113 is due to multiple polarized components blended within the beam.

Multiple emission components are also supported by the lack of clear periodic modulation in the X-ray and VHE data, which is seen in most of the other wavelengths. On the other hand, the short-term variability in all bands is clearly correlated on some occasions (for example, data around MJD 57 000 in Fig. 7 connecting optical and X-ray emission), while at other times there can even be an anticorrelation (data around MJD 57 500 in the same figure). This shows that the situation is very complex. The difficulty to connect the low-energy part of the synchrotron bump (IR/optical/UV) to the high-energy synchrotron part (X-rays) was extensively studied in Raiteri et al. (2015). They studied the synchrotron spectrum of the source in multiple activity states and found that the changes in the spectrum can be explained with an inhomogeneous helical jet model, where the high-energy emission originates closer to the black hole than the low-energy emission. Alternatively, there could be multiple (disconnected) emission components or a more complex electron distribution than typically assumed.

Our analyses on the periodicity show that there clearly must be multiple components contributing to the emission, but that they also cannot be fully disconnected because we (at least sometimes) see simultaneous flaring in all bands. Moreover, the minima in the folded light curves seem to be in phase in all bands. Some of the bands (X-ray and VHE) may be more sensitive to the stochastic variations only, while in the other wavelengths, connected with the low-energy part of the SED peaks, we can also see the periodic modulation. This means that any model explaining the periodicity should also be able to explain why it is more prominent in the low-energy part. Confirming this discrepancy would also require longer, densely sampled, light curves in X-ray and VHE energies.

ACKNOWLEDGEMENTS

We would like to thank the Instituto de Astrofísica de Canarias for the excellent working conditions at the Observatorio del Roque de los Muchachos in La Palma. The financial support of the German BMBF, MPG, and HGF; the Italian INFN and INAF; the Swiss National Fund SNF; the grants PID2019-104114RB-C31, PID2019-104114RB-C32, PID2019-104114RB-C33, PID2019-105510GB-C31, PID2019-107847RB-C41, PID2019-107847RB-C42, PID2019-107847RB-C44, PID2019-107988GB-C22, PID2020-118491GB-I00 funded by the Spanish MCIN/AEI/ 10.13039/501100011033; the Indian Department of Atomic Energy; the Japanese ICRR, the University of Tokyo, JSPS, and MEXT; the Bulgarian Ministry of Education and Science, National RI Roadmap Project DO1-400/18.12.2020 and the Academy of Finland grant nr. 320045 is gratefully acknowledged. This work was also been supported by Centros de Excelencia ‘Severo Ochoa’ y Unidades ‘María de Maeztu’ program of the Spanish MCIN/AEI/ 10.13039/501100011033 (SEV-2016-0588, CEX2019-000920-S, CEX2019-000918-M, CEX2021-001131-S, MDM-2015-0509-18-2) and by the CERCA institution of the Generalitat de Catalunya; by the Croatian Science Foundation (HrZZ) Project IP-2016-06-9782 and the University of Rijeka Project uniri-prirod-18-48; by the Deutsche Forschungsgemeinschaft (SFB1491 and SFB876); the Polish Ministry Of Education and Science grant No. 2021/WK/08; and by the Brazilian MCTIC, CNPq and FAPERJ. EP acknowledges funding from Italian Ministry of Education,

University and Research (MIUR) through the ‘Dipartimenti di eccellenza’ project Science of the Universe. TH was supported by the Academy of Finland projects 317383, 320085, 322535, and 345899. The Liverpool Telescope is operated on the island of La Palma by Liverpool John Moores University in the Spanish Observatorio del Roque de los Muchachos of the Instituto de Astrofísica de Canarias with financial support from the UK Science and Technology Facilities Council. Data was used from Steward Observatory blazar spectropolarimetric monitoring project, which was supported by NASA Fermi Guest Investigator Grants NNX09AU10G, NNX12AO93G, and NNX15AU81G. DB acknowledges support from the European Research Council (ERC) under the European Union Horizon 2020 research and innovation program under the grant agreement No 771282. GD and OV acknowledge support by the Astronomical station Vidojevica, funding from the Ministry of Science, Technological Development and Innovation of the Republic of Serbia (contract No. 451-03-47/2023-01/200002), by the EC through project BELISSIMA (call FP7-REGPOT-2010-5, No. 265772), the observing and financial grant support from the Institute of Astronomy and Rozhen NAO BAS through the bilateral SANU-BAN joint research project GAIA ASTROMETRY AND FAST VARIABLE ASTRONOMICAL OBJECTS, and support by the SANU project F-187. The Abastumani team acknowledges financial support by the Shota Rustaveli NSF of Georgia under contract FR-19-6174. This research was partially supported by the Bulgarian National Science Fund of the Ministry of Education and Science under grants DN 18–13/2017, KP-06-H28/3 (2018), KP-06-H38/4 (2019) and KP-06-KITAJ/2 (2020). We acknowledge support by Bulgarian National Science Fund under grant DN18-10/2017 and National RI Roadmap Projects D01-383/18.12.2020 of the Ministry of Education and Science of the Republic of Bulgaria. The research at Boston University was supported by NASA Fermi Guest Investigator Program grants 80NSSC22K1571 and 80NSSC23K1507. This study used observations conducted with the 1.8m Perkins Telescope (PTO) in Arizona (USA), which is owned and operated by Boston University. This research has made use of data from the OVRO 40-m monitoring program (Richards, J. L. et al. 2011, *ApJS*, 194, 29), supported by private funding from the California Institute of Technology and the Max Planck Institute for Radio Astronomy, and by NASA grants NNX08AW31G, NNX11A043G, and NNX14AQ89G and NSF grants AST-0808050 and AST-1109911. WM gratefully acknowledges support by the ANID BASAL project FB210003 and FONDECYT 11190853. SK acknowledges support from the European Research Council (ERC) under the European Unions Horizon 2020 research and innovation programme under grant agreement No. 771282. RR acknowledges support from ANID BASAL projects ACE210002 and FB210003, and ANID Fondecyt 1181620. RL acknowledges financial support from the State Agency for Research of the Spanish MCIU through the ‘Center of Excellence Severo Ochoa’ award to the Instituto de Astrofísica de Andalucía (SEV-2017-0709).

DATA AVAILABILITY

The data underlying this article will be shared on reasonable request to the corresponding authors.

REFERENCES

- Abramowski A. et al., 2015, *ApJ*, 802, 65
 Acciari V. A. et al., 2019, *MNRAS*, 486, 4233
 Acciari V. A. et al., 2020, *ApJS*, 247, 16
 Acciari V. A. et al., 2021, *MNRAS*, 504, 1427
 Ackermann M. et al., 2015, *ApJ*, 813, L41
 Agarwal A. et al., 2021, *A&A*, 645, A137
 Ait Benkhali F., Hofmann W., Rieger F. M., Chakraborty N., 2020, *A&A*, 634, A120
 Albert J. et al., 2007, *ApJ*, 669, 862
 Aleksić J. et al., 2011, *ApJ*, 730, L8
 Aleksić J. et al., 2012, *ApJ*, 748, 46
 Aleksić J. et al., 2015, *MNRAS*, 450, 4399
 Aleksić J. et al., 2016a, *Astropart. Phys.*, 72, 61
 Aleksić J. et al., 2016b, *Astropart. Phys.*, 72, 76
 Aliu E. et al., 2015, *ApJ*, 799, 7
 Baars J. W. M., Genzel R., Pauliny-Toth I. I. K., Witzel A., 1977, *A&A*, 61, 99
 Baixeras C. et al., 2004, *Nucl. Instrum. Methods Phys. Res. A*, 518, 188
 Bhatta G., 2017, *ApJ*, 847, 7
 Blinov D. et al., 2021, *MNRAS*, 501, 3715
 Burrows D. N. et al., 2005, *Space Sci. Rev.*, 120, 165
 Camenzind M., Krockenberger M., 1992, *A&A*, 255, 59
 Caproni A., Abraham Z., Motter J. C., Monteiro H., 2017, *ApJ*, 851, L39
 Conway J. E., Murphy D. W., 1993, *ApJ*, 411, 89
 Covino S. et al., 2004, in Moorwood A. F. M., Iye M. eds, *Proc. SPIE Conf. Ser. Vol. 5492, Ground-based Instrumentation for Astronomy*. SPIE, Bellingham, p. 1613
 Covino S., Sandrinelli A., Treves A., 2019, *MNRAS*, 482, 1270
 Covino S., Landoni M., Sandrinelli A., Treves A., 2020, *ApJ*, 895, 122
 Czesla S., Schröter S., Schneider C. P., Huber K. F., Pfeifer F., Andreason D. T., Zechmeister M., 2019, *Astrophysics Source Code Library, record(asc1:1906.010)*
 Danforth C. W., Keeney B. A., Stocke J. T., Shull J. M., Yao Y., 2010, *ApJ*, 720, 976
 Danforth C. W. et al., 2016, *ApJ*, 817, 111
 Dey L. et al., 2018, *ApJ*, 866, 11
 Dhiman V., Gupta A. C., Gaur H., Wiita P. J., 2021, *MNRAS*, 506, 1198
 Dorigo Jones J. et al., 2022, *MNRAS*, 509, 4330
 Falomo R., Pian E., Treves A., 2014, *A&AR*, 22, 73
 Fitzpatrick E. L., 1999, *PASP*, 111, 63
 Gehrels N. et al., 2004, *ApJ*, 611, 1005
 Giroletti M., Righini S., 2020, *MNRAS*, 492, 2807
 Guo J., Li H.-J., Bi X.-J., Lin S.-J., Yin P.-F., 2020, preprint (arXiv:2002.07571)
 Gupta A. C. et al., 2016, *MNRAS*, 458, 1127
 Haehnelt M. G., Rees M. J., 1993, *MNRAS*, 263, 168
 Honma F., Matsumoto R., Kato S., 1992, *PASJ*, 44, 529
 Hovatta T., Lindfors E., 2019, *New Astron. Rev.*, 87, 101541
 Hovatta T. et al., 2016, *A&A*, 596, A78
 Jermak H. et al., 2016, *MNRAS*, 462, 4267
 Johnson S. D. et al., 2019, *ApJ*, 884, L31
 Jorstad S. G. et al., 2010, *ApJ*, 715, 362
 Kalberla P. M. W., Burton W. B., Hartmann D., Arnal E. M., Bajaja E., Morras R., Pöppel W. G. L., 2005, *A&A*, 440, 775
 Konar C., Hardcastle M. J., Jamroz M., Croston J. H., 2013, *MNRAS*, 430, 2137
 Korochkin A., Neronov A., Semikoz D., 2020, *A&A*, 633, A74
 Larionov V. M. et al., 2008, *A&A*, 492, 389
 Lehto H. J., Valtonen M. J., 1996, *ApJ*, 460, 207
 Lico R. et al., 2020, *A&A*, 634, A87
 Liodakis I., Romani R. W., Filippenko A. V., Kiehlmann S., Max-Moerbeck W., Readhead A. C. S., Zheng W., 2018, *MNRAS*, 480, 5517
 Liodakis I., Romani R. W., Filippenko A. V., Kocevski D., Zheng W., 2019, *ApJ*, 880, 32
 MAGIC Collaboration, 2018, *MNRAS*, 480, 879
 Marscher A. P., 2016, *Galaxies*, 4
 Nilsson K. et al., 2018, *A&A*, 620, A185
 O’Neill S. et al., 2022, *ApJ*, 926, L35
 Peñil P. et al., 2020, *ApJ*, 896, 134
 Perley R. A., Butler B. J., 2013, *ApJS*, 204, 19
 Pian E. et al., 1998, *ApJ*, 492, L17

- Poole T. S., Breeveld A. A., 2005, Swift UVOT calibration document SWIFT-UVOT-CALDB-02-R03: Count Rate to Flux Ratio. Available at: <https://heasarc.gsfc.nasa.gov/docs/heasarc/caldb/swift/docs/uvot/>
- Poole T. S., Breeveld A. A., Landsman W., 2005, Swift UVOT CALDB Release Note Swift-Uvot-Caldb-01-R04: Zero Points. Available at: <https://heasarc.gsfc.nasa.gov/docs/heasarc/caldb/swift/docs/uvot/>
- Poole T. S. et al., 2008, *MNRAS*, 383, 627
- Prokhorov D. A., Moraghan A., 2017, *MNRAS*, 471, 3036
- Raiteri C. M. et al., 2015, *MNRAS*, 454, 353
- Raiteri C. M. et al., 2017a, *MNRAS*, 466, 3762
- Raiteri C. M. et al., 2017b, *Nature*, 552, 374
- Richards J. L. et al., 2011, *ApJS*, 194, 29
- Rieger F. M., 2004, *ApJ*, 615, L5
- Rieger F., 2019, *Galaxies*, 7, 28
- Rieger F. M., Mannheim K., 2000, *A&A*, 359, 948
- Romero G. E., Chajet L., Abraham Z., Fan J. H., 2000, *A&A*, 360, 57
- Roming P. W. A. et al., 2005, *Space Sci. Rev.*, 120, 95
- Sandrinelli A., Covino S., Treves A., 2014, *A&A*, 562, A79
- Sandrinelli A., Covino S., Treves A., Holgado A. M., Sesana A., Lindfors E., Ramazani V. F., 2018, *A&A*, 615, A118
- Scargle J. D., Norris J. P., Jackson B., Chiang J., 2013, *ApJ*, 764, 167
- Schlaflly E. F., Finkbeiner D. P., 2011, *ApJ*, 737, 103
- Skrutskie M. F. et al., 2006, *AJ*, 131, 1163
- Smith P. S., Montiel E., Rightley S., Turner J., Schmidt G. D., Jannuzi B. T., 2009, preprint ([arXiv:0912.3621](https://arxiv.org/abs/0912.3621))
- Sobacchi E., Sormani M. C., Stamerra A., 2017, *MNRAS*, 465, 161
- Takalo L. O., Nilsson K., Lindfors E., Sillanpää A., Berdyugin A., Pasanen M., 2008, in Aharonian A. F., Hofmann W., Rieger F., eds, *Proc. AIP Conf. Ser. Vol. 1085, High Energy Gamma-ray Astronomy*. Am Inst. Phys., New York, p.705
- Tavani M., Cavaliere A., Munar-Adrover P., Argan A., 2018, *ApJ*, 854, 11
- Tavecchio F., Maraschi L., Ghisellini G., 1998, *ApJ*, 509, 608
- Tchekhovskoy A., Narayan R., McKinney J. C., 2011, *MNRAS*, 418, L79
- Ulrich M.-H., Maraschi L., Urry C. M., 1997, *ARA&A*, 35, 445
- Uttley P., McHardy I. M., Papadakis I. E., 2002, *MNRAS*, 332, 231
- Vaughan S., Edelson R., Warwick R. S., Uttley P., 2003, *MNRAS*, 345, 1271
- Villata M., Raiteri C. M., 1999, *A&A*, 347, 30
- Villata M. et al., 2002, *A&A*, 390, 407
- Wardle J. F. C., Kronberg P. P., 1974, *ApJ*, 194, 249
- Wilms J., Allen A., McCray R., 2000, *ApJ*, 542, 914
- Zanin R. et al., 2013, *Proceedings of the 33rd International Cosmic Ray Conference (ICRC 2013)*. Sociedade Brasileira de Fisica, Brazil, p. 2937
- Zechmeister M., Kürster M., 2009, *A&A*, 496, 577
- Zerbi F. M. et al., 2004, in Moorwood A. F. M., Iye M. eds, *Proc. SPIE Conf. Ser. Vol. 5493, Ground-based Instrumentation for Astronomy*. SPIE, Bellingham, p. 1590
- ¹Japanese MAGIC Group: Institute for Cosmic Ray Research (ICRR), The University of Tokyo, Kashiwa, 277-8582 Chiba, Japan
- ²ETH Zürich, CH-8093 Zürich, Switzerland
- ³Instituto de Astrofísica de Canarias and Departamento de Astrofísica, Universidad de La Laguna, E-38200 La Laguna, Tenerife, Spain
- ⁴Instituto de Astrofísica de Andalucía-CSIC, Glorieta de la Astronomía s/n, E-18008 Granada, Spain
- ⁵National Institute for Astrophysics (INAF), I-00136 Rome, Italy
- ⁶INFN Trieste, Università di Udine, I-33100 Udine, Italy
- ⁷International Center for Relativistic Astrophysics (ICRA), I-00185 Rome, Italy
- ⁸Institute for Nuclear Research and Nuclear Energy, Bulgarian Academy of Sciences, BG-1784 Sofia, Bulgaria
- ⁹INFN, Università di Padova, I-35131 Padova, Italy
- ¹⁰Institut de Física d'Altes Energies (IFAE), The Barcelona Institute of Science and Technology, E-08193 Bellaterra (Barcelona), Spain
- ¹¹Technische Universität Dortmund, D-44221 Dortmund, Germany
- ¹²Croatian MAGIC Group: University of Zagreb, Faculty of Electrical Engineering and Computing (FER), 10000 Zagreb, Croatia
- ¹³IPARCOS Institute and EMFTEL Department, Universidad Complutense de Madrid, E-28040 Madrid, Spain
- ¹⁴Centro Brasileiro de Pesquisas Físicas (CBPF), 22290-180 URCA, Rio de Janeiro (RJ), Brazil
- ¹⁵Centro de Investigaciones Energéticas, Medioambientales y Tecnológicas, E-28040 Madrid, Spain
- ¹⁶Departament de Física, and CERES-IEEC, Universitat Autònoma de Barcelona, E-08193 Bellaterra, Spain
- ¹⁷INFN Pisa, Università di Pisa, I-56126 Pisa, Italy
- ¹⁸ICCUB, IEEC-UB, Universitat de Barcelona, E-08028 Barcelona, Spain
- ¹⁹INFN MAGIC Group: INFN Sezione di Catania and Dipartimento di Fisica e Astronomia, University of Catania, I-95123 Catania, Italy
- ²⁰Institute for Astro- and Particle Physics, University of Innsbruck, A-6020 Innsbruck, Austria
- ²¹Department for Physics and Technology, University of Bergen, 5007 Bergen, Norway
- ²²Port d'Informació Científica (PIC), E-08193 Bellaterra (Barcelona), Spain
- ²³INFN MAGIC Group: INFN Sezione di Torino and Università degli Studi di Torino, I-10125 Torino, Italy
- ²⁴INFN MAGIC Group: INFN Sezione di Bari and Dipartimento Interateneo di Fisica dell'Università e del Politecnico di Bari, I-70125 Bari, Italy
- ²⁵Croatian MAGIC Group: University of Rijeka, Faculty of Physics, 51000 Rijeka, Croatia
- ²⁶Hans-Haffner-Sternwarte, Naturwissenschaftliches Labor für Schüler am FKG, Friedrich-Koenig-Gymnasium, D-97082 Würzburg, Germany
- ²⁷University of Geneva, Chemin d'Ecogia 16, CH-1290 Versoix, Switzerland
- ²⁸Japanese MAGIC Group: Physics Program, Graduate School of Advanced Science and Engineering, Hiroshima University, 739-8526 Hiroshima, Japan
- ²⁹Armenian MAGIC Group: ICRANet-Armenia, 0019 Yerevan, Armenia
- ³⁰Faculty of Physics and Applied Informatics, Department of Astrophysics, University of Lodz, 90-236 Lodz, Poland
- ³¹Institute for Astro- and Particle Physics, University of Innsbruck, A-6020 Innsbruck, Austria
- ³²Finnish MAGIC Group: Finnish Centre for Astronomy with ESO, University of Turku, FI-20014 Turku, Finland
- ³³Aalto University Metsähovi Radio Observatory, Metsähovintie 114, FI-02540 Kylmälahti, Finland
- ³⁴Croatian MAGIC Group: Josip Juraj Strossmayer University of Osijek, Department of Physics, 31000 Osijek, Croatia
- ³⁵Universität Würzburg, D-97074 Würzburg, Germany
- ³⁶Department of Physics, University of Oslo, Norway
- ³⁷Japanese MAGIC Group: Department of Physics, Tokai University, Hiratsuka, 259-1292 Kanagawa, Japan
- ³⁸NASA Marshall Space Flight Center, Huntsville, AL 35812, USA
- ³⁹Dipartimento di Fisica, Università di Trieste, I-34127 Trieste, Italy
- ⁴⁰INFN Pisa, Università di Siena, I-53100 Siena, Italy
- ⁴¹Saha Institute of Nuclear Physics, A CI of Homi Bhabha National Institute, Kolkata 700064, West Bengal, India
- ⁴²Max-Planck-Institut für Physik, D-80805 München, Germany
- ⁴³Max-Planck-Institut für Physik, D-80805 München, Germany
- ⁴⁴Japanese MAGIC Group: Department of Physics, Yamagata University, Yamagata 990-8560, Japan
- ⁴⁵Finnish MAGIC Group: Space Physics and Astronomy Research Unit, University of Oulu, FI-90014 Oulu, Finland
- ⁴⁶Japanese MAGIC Group: Chiba University, ICEHAP, 263-8522 Chiba, Japan
- ⁴⁷Japanese MAGIC Group: Institute for Space-Earth Environmental Research and Kobayashi-Maskawa Institute for the Origin of Particles and the Universe, Nagoya University, 464-6801 Nagoya, Japan
- ⁴⁸INAF, Osservatorio Astronomico di Padova, I-35122, Padova, Italy
- ⁴⁹Japanese MAGIC Group: Department of Physics, Kyoto University, 606-8502 Kyoto, Japan
- ⁵⁰Japanese MAGIC Group: Institute for Cosmic Ray Research (ICRR), The University of Tokyo, Kashiwa, 277-8582 Chiba, Japan
- ⁵¹INFN MAGIC Group: INFN Sezione di Perugia, I-06123 Perugia, Italy
- ⁵²INFN MAGIC Group: INFN Roma Tor Vergata, I-00133 Roma, Italy
- ⁵³Japanese MAGIC Group: Department of Physics, Konan University, Kobe, Hyogo 658-8501, Japan
- ⁵⁴Astrophysics Research Institute, Liverpool John Moores University, and Liverpool Science Park, 146 Brownlow Hill, Liverpool L3 5RF, UK

- ⁵⁵Steward Observatory, University of Arizona, Tucson, AZ 85721, USA
⁵⁶Institute of Astrophysics, Foundation for Research and Technology—Hellas, Voutes, 7110 Heraklion, Greece
⁵⁷Department of Physics, University of Crete, 71003 Heraklion, Greece
⁵⁸INAF, Osservatorio Astrofisico di Torino, via Osservatorio 20, I-10025 Pino Torinese, Italy
⁵⁹Ulugh Beg Astronomical Institute, Astronomy Street 33, Tashkent 100052, Uzbekistan
⁶⁰Abastumani Observatory, Mt. Kanobili, 0301 Abastumani, Georgia
⁶¹Landessternwarte, Zentrum für Astronomie der Universität Heidelberg, Königstuhl 12, D-69117 Heidelberg, Germany
⁶²EPT Observatories, Tijarafe, E-38780 La Palma, Spain and , Spain
⁶³INAF, TNG Fundación Galileo Galilei, E-38712 La Palma, Spain
⁶⁴Saint Petersburg State University, 7/9 Universitetskaya nab., St. Petersburg, 199034 Russia
⁶⁵Special Astrophysical Observatory, Russian Academy of Sciences, 369167, Nizhnii Arkhyz, Russia and Pulkovo Observatory, St.Petersburg, 196140, Russia
⁶⁶Crimean Astrophysical Observatory RAS, P/O Nauchny, 298409, Crimea
⁶⁷Department of Astronomy, Faculty of Physics, University of Sofia, BG-1164 Sofia, Bulgaria
⁶⁸Astronomical Observatory, Volgina 7, 11060 Belgrade, Serbia
⁶⁹National University of Uzbekistan, Tashkent 100174, Uzbekistan
⁷⁰INAF, Istituto di Radioastronomia, via Gobetti 101, I-40129 Bologna, Italy
⁷¹Department of Physics and Astronomy, Faculty of Natural Sciences, University of Shumen, BG-9712 Shumen, Bulgaria

- ⁷²Institute for Astrophysical Research, Boston University, 725 Commonwealth Avenue, Boston, MA 02215, USA
⁷³Engelhardt Astronomical Observatory, Kazan Federal University, Tatarstan, Russia
⁷⁴Astronomical Observatory, Department of Physical Sciences, Earth and Environment, University of Siena, I-53100, Siena, Italy
⁷⁵Institute of Astronomy and National Astronomical Observatory, Bulgarian Academy of Sciences, 1784 Sofia, Bulgaria
⁷⁶Department of Physics, University of Colorado Denver, Denver, Colorado 80204, USA
⁷⁷Owens Valley Radio Observatory, California Institute of Technology, Pasadena, CA 91125, USA
⁷⁸Departamento de Astronomía, Universidad de Chile, Camino El Observatorio 1515, Las Condes, Santiago, Chile
⁷⁹CePIA, Departamento de Astronomía, Universidad de Concepción, 4030000 Concepción, Chile
⁸⁰INAF, Osservatorio Astronomico di Brera, Via E. Bianchi 46, I-23807 Merate, Italy
⁸¹Aryabhata Research Institute of Observational Sciences (ARIES), Manora Park, Nainital 263 001, India
⁸²INFN – Sezione di Milano-Bicocca, piazza della Scienza 3, I-20126 Milano (MI), Italy

This paper has been typeset from a \LaTeX file prepared by the author.